Vibration Detection In Turbomachinery Using Non-Contacting Sensors

by

Eric D. Cohen

Submitted to the Department of Electrical Engineering and Computer Science
in partial fulfillment of the requirements for the degree of

Master of Engineering in Electrical Engineering and Computer Science

at the

MASSACHUSETTS INSTITUTE OF TECHNOLOGY

June 2006]
May 26, 2006

Author..............................
Department of Electrical Engineering and Computer Science
May 26, 2006

Certified by..............................
James D. Paduano
Thesis Supervisor

Accepted by..............................
Arthur C. Smith
Chairman, Department Committee on Graduate Theses

[redacted]

Vibration Detection In Turbomachinery Using Non-Contacting Sensors

by

Eric D. Cohen

Submitted to the Department of Electrical Engineering and Computer Science
on May 26, 2006, in partial fulfillment of the
requirements for the degree of
Master of Engineering in Electrical Engineering and Computer Science

Abstract

Recent developments have seen the introduction of multiple Eddy Current Sensors (ECS) into turbomachinery. These sensors employ an active magnetic field to monitor each blade as it passes the sensor. They generate an electrical signal proportional to the distance of a blade from the sensor. Existing algorithms extract two pieces of information from the ECS signature, signal magnitude and signal zero crossing time. The signal magnitude is used to find tip clearance, and the zero crossing time is used to estimate vibrational parameters over the course of multiple revolutions. These techniques fail to exploit the majority of the information contained in the ECS signal.

In this research, a novel residue characterization algorithm was developed that processes the full ECS pulse to produce a residue. The residue is a speed independent representation of differences between a baseline ECS pulse and an experimental ECS pulse. A mathematical model of the relationship between blade displacement and residue was developed. Empirical data collected with the MIT spin pit were used to verify convergence of the model with the residue characterization algorithm. This strongly suggests blade vibration can be deduced using the residue characterization method with a single ECS sensor.

Thesis Supervisor: James D. Paduano
Title: Principal Research Engineer of Aeronautics and Astronautics

Acknowledgments

I would first like to offer my profound gratitude to my adviser, Dr. James D. Paduano, without whom this work would not have been possible. He has been a consistent source of guidance, advice, and support.

I would like thank my undergraduate assistant, Nabori Santiago, whose many hours of assistance with data collection helped make this research possible.

I thank Boeing/Rocketdyne for supporting this research, particularly John Vian for initiating the project, and Sarkis Barkhoudarian and Roland Szabo for their help in characterizing the Mk3 blisk.

I am very grateful to all of the people at MIT and GTL who have helped me along the way including Jimmy Letendre, Jack Costa, John Kane, E. Paul Warren, and Holly Anderson.

I also extend many thanks to all of my good friends, particularly Jaydeep Bardhan for his empathy, advice, and distraction, Fernando Ceballos for the Mariachi music, Andrew Martinez for the cases, and Brian "PS" Savery for his early morning wisdom.

I am extremely grateful to Mugsie Burkshire, who gave me my first "real" computer, and to Nick Burkshire for the hover board plans.

Words cannot convey my most profound gratitude to my entire wonderful family, especially my parents Cheryl Jones and Stewart Cohen, to whom I owe everything, my brother Andrew Cohen, who I am watching grow into a fine young man, my grandmother Rudy Cohen, whose youth is inspiring, my grandfather Albert Cohen, who fought for this country, my grandmother Jackie Klarman, whose indomitable spirit is extraordinary, and my grandfather Harold Klarman, who literally sparked my interest in science and technology.

Contents

List of Figures

List of Tables

Chapter 1

Introduction

Jet engine technology is the mainstay of the air transit industry. This technology is based upon the burning of fuel in an environment of intense heat and pressure. To achieve the conditions necessary for combustion, a sequence of rotor stages rotate at extremely high speeds to compress incoming air. The compressor stage is driven by the "hot section", which consists of a turbine spun by high speed exhaust gasses emanating from the combustor.

Liquid fueled rocket engines employ a related technology called turbopumps to pump the vast quantities of fuel they require. Turbopumps are powered by hot exhaust gasses passing over a turbine wheel. Much like a turbocharger in an automobile, this turbine is mechanically connected to a pump. In the case of a rocket engine, the pump is pumping liquid fuel instead of air. These pumps are susceptible to the same types of failure as jet aircraft engines.

As the machinery rotates, the turbine blades tend to vibrate. These vibrations induce stresses in the blades. These stresses can eventually lead to a failure condition known as high-cycle fatigue failure (HCF). This type of failure may initially manifest itself as small cracks. Over time, the crack propagates, and eventually leads to catastrophic failure of the rotating machinery. Since these components rotate at over 10,000RPM, there is sufficient energy for the debris to penetrate the fuselage of an aircraft and cause injury or death to passengers. In the worst case, such a failure can bring down an entire aircraft, or cause the loss of a launch vehicle. Real-time knowledge of turbine blade vibration is critical to predicting and preventing such failures.

While HCF failure is perhaps the most insidious failure mode, turbomachinery is also susceptible to more rapid forms of failure. For example, foreign object damage (FOD), where a jet engine ingests debris such as pebbles, has led to a number of high profile incidents. Engines can also be damaged by out of balance conditions and accessory failures. These are among the many turbomachinery failure modes that can be detected and possibly prevented through blade vibration monitoring.

1.1 Overview

In this research, I will be investigating the use of eddy current sensors (ECS) and variable reluctance sensors (VRS) in determining vibration in turbomachinery components. These sensors detect the passing blade tip using an active magnetic field in the case of ECS and a passive field in the case of VRS. The resulting signal contains, indirectly, information pertaining to the vibration of the blades.

This work can be classified into two primary sections, the experimental stage and the data reduction stage. The experimental stage consists of spinning test articles in a spin pit and collecting data from a combination of tachometer, ECS sensors, VRS sensors, and strain gages. In the data reduction stage, the data are analyzed using a number of different algorithms. The strain gage data provide a complete picture of actual blade behavior and are used to quantitatively evaluate algorithm performance using data from the non-contacting sensors.

1.1.1 Current NSMS Methods

ECS sensors are currently deployed in the F-35 Joint Strike Fighter engine. However, they are used only to monitor blade tip clearance, which is derived by simply taking the maximum value of each ECS pulse. All other data in the ECS pulse are discarded. Most current NSMS (Non-Contact Stress Measurement System) research is primarily focused on a technique known as tip timing [4]. Tip timing systems generally employ special hardware to accurately measure the time at which an ECS pulse passes through zero volts. Since vibrating blades arrive at the sensor at slightly different times, the time of zero crossing is also slightly different, depending on the vibration characteristics [4]. These small timing differences allow blade vibration to be inferred.

Tip timing has a number of deficiencies. It is an inherently aliased approach, since effectively only a single sample per revolution is taken from each blade. Thus, resolving blade vibration often requires multiple sensors. More recent techniques are being devised for single sensor use, however they require multiple revolutions of the rotor to even begin to deduce blade behavior [4]. Like the clearance monitoring systems currently deployed, tip timing fails to exploit the majority of the data available in an ECS waveform.

1.2 Proposed System

An algorithm stack that deduces turbine blade vibration using full ECS waveform analysis is proposed (Figure 1-1). Data from the ECS sensor are first passed to an adaptive filter, which computes a constantly updated historic model of the ECS waveform. The modeled ECS wave and the current ECS wave are then processed with a residue characterization algorithm. Finally, the resulting residue is interpreted using a synthesis algorithm. The synthesis algorithm translates the residue into blade dynamics parameters.

1.3 Algorithms

In this research, algorithms were developed that exploit the entire ECS waveform from a single sensor. The first algorithm applied was the short time Fourier transform, which is a widely used standard method for analyzing the frequency content of a signal. Next, Hilbert transform algorithms were investigated. Although the Hilbert transform is classic mathematical technique, only recently has it been ap-

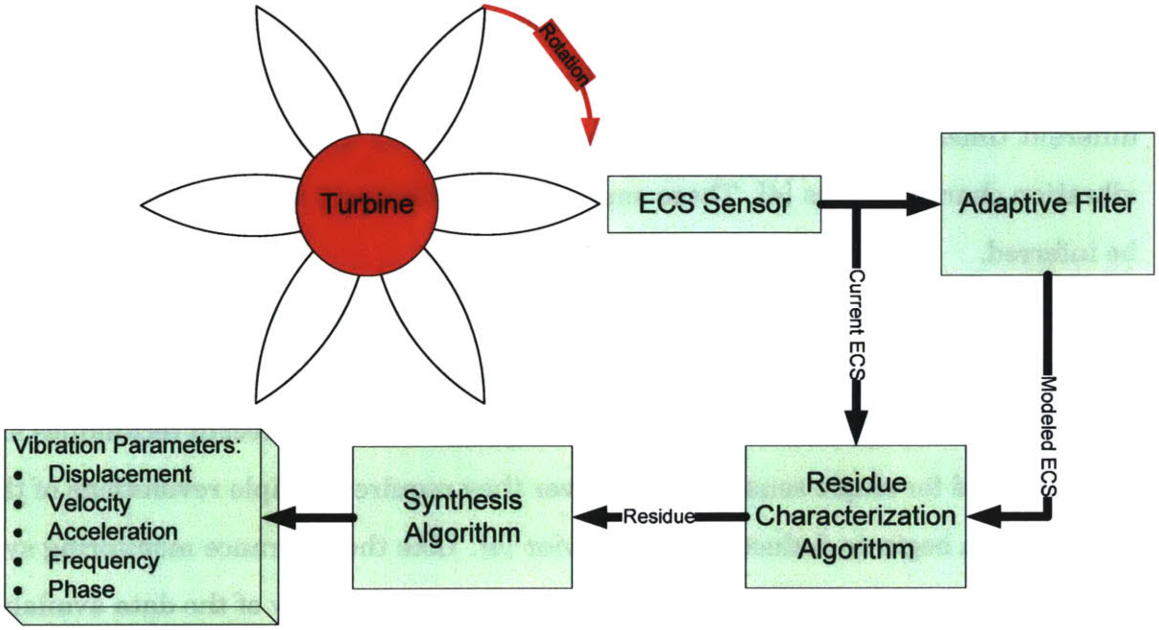

Figure 1-1: Block diagram of proposed blade vibration detection system.

plied to turbomachinery vibration detection. The third algorithm employed was the residue characterization method, which is a novel algorithm developed specifically for this research. Finally, an adaptive filter algorithm was investigated as a means of preprocessing multiple revolutions of data for analysis using the residue characterization method.

1.3.1 Short Time Fourier Transform

All data were first analyzed using a short time Fourier transform method. This generates spectrogram plots which show the time evolution of the frequency content of the data. The spectrogram plot provides a convenient means of identifying blade resonances during a run, characterizing the noise spectrum, and selecting data sets and ranges for further analysis. An automated suite of scripts was developed to process raw data and generate a series of spectrogram plots for each sensor.

1.3.2 Hilbert Transform

The Hilbert transform is equivalent to a Fourier transform with its negative frequencies zeroed. It can be used to derive a complex-valued analytic signal. From the analytic signal, "instantaneous frequency", which is an approximation of frequency at a particular moment in time, can be calculated. By finding the instantaneous frequency of each point within a window of ECS data, an approximation of frequency content as a function of time is found.

1.3.3 Residue Characterization Method

Unlike Fourier and Hilbert transform methods, which are rooted in the frequency domain, residue characterization methods are based strictly in the time domain. After applying a number of preparatory signal processing steps, including rotor speed correction, residue characterization directly compares a baseline ECS pulse with an unknown ECS pulse. The resulting residue shows the difference between the two signals. To assist in interpreting features of the residue, a model was developed to estimate the expected residue resulting from individual component changes in tip clearance, arrival time, velocity, and acceleration. Since real world data exhibit a combination of these component changes simultaneously, a more advanced simulator was subsequently created to estimate their combined effects.

1.3.4 Adaptive Filter

Adaptive filters tune their filter coefficients in real-time to minimize an error function. For this research, an LMS adaptive filter was employed to derive a historic model of an ECS pulse. By tuning the adaption rate, the filter can adapt the model to an arbitrarily large or small number of ECS pulses, which mitigates uncorrelated noise while still reflecting the time evolution of the ECS signal. The error signal from the filter reflects how the current ECS pulse differs from the adaptive model.

1.4 Thesis Outline

- Chapter 2 describes the experimental setup, including operation and maintenance of the spin pit, operating constraints, data acquisition equipment, amplifiers, sensors, and magnets.
- Chapter 3 details data collection methods. These include test plan development, sample rates, sweep rates, and sensor calibration. The two test articles and their characteristics are also described.
- Chapter 4 discusses the four algorithms used for data reduction and analysis. Each is covered individually and evaluated. The residue model and simulator are also covered in this section. Graphical results from each method applied to experimental data follow, along with predicted results.
- Chapter 5 summarizes the research, and provides direction and recommendations for future work.

Chapter 2

Experimental Setup

Simulating the operation of turbomachinery requires an extensive experimental setup. Everything revolves around the spin pit, which is an armored, motorized vacuum chamber designed to safely spin test articles at high speeds. ECS and VRS sensors are mounted around the perimeter of the spin pit on traverses with their leads exiting the spin pit through a vacuum pass-through. On-rotor strain gages pass their signals from the spin pit via a slip ring.

Once out of the spin pit, the various signals travel through a number of amplifiers and data collection devices. For the ECS sensors, this involves passing through a demodulator [5], a common mode rejection amplifier, order tracking equipment and tip timing equipment provided by Hood Technologies, and finally terminating in a digital-to-analog converter (DAQ). The strain gage signals pass through a bank of conditioning amplifiers and then to the DAQ.

2.1 Spin Pit

The spinning of a turbine blade in an engine is simulated in an apparatus known as a spin pit (Figure 2-1). The spin pit consists of a variable speed electric motor with a shaft terminating inside an evacuated chamber. The test article is mounted on this shaft, and the spin pit sealed. A vacuum is then drawn, and the spin pit is ready for operation. Any speed between 0-20,000RPM can be programmed into the motor controller, along with an acceleration profile. To stimulate excitation of the blades, high power magnet modules can be installed in the pit (Section 2.1.4).

2.1.1 Operating Constraints

The spin pit has a number of serious limitations. Chief among these are thermal constraints. The interface between the drive shaft and the rotor is sealed by a carbon face seal. This seal is held against a plate on the lower section of the rotor, and is the highest friction point in the system. Especially at higher speeds (5,000 RPM and higher), temperature rises rapidly. Since it is not possible to mount a conventional thermocouple on the carbon seal itself, one is mounted on the seal housing. This thermocouple reading is monitored so as not to exceed 100 degrees Fahrenheit, which we estimate corresponds to about 200 degrees on the carbon seal itself. Using this limitation, approximately 20 seconds of run time is achievable at 6,000 RPM and approximately 180 seconds at 3,000 RPM.

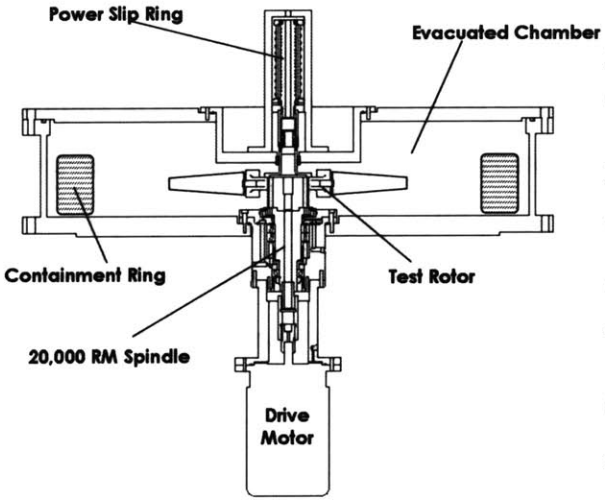

Figure 2-1: Diagram of spin pit.

The spindle of the spin pit is supported by three ABEC-9 thrust bearings. Two of these bearings are setup as a duplex pair at the top of the spindle, and the remaining smaller bearing is mounted on the lower part of the shaft. The lower bearing is preloaded by a spring web consisting of 24 small, rigid springs. Bearing temperature is critical, and monitored with a pair of thermocouples protruding into the bearing housing. To maintain the integrity of the bearing housing, the thermocouple holes do not penetrate the housing, so the thermocouples do not actually contact the bearing races. Like the face seal, this necessitates a conservative approach to temperature monitoring. The bearings are heat stabilized to 350 degrees Fahrenheit, so a conservative maximum thermocouple reading has been estimated to be 150 degrees Fahrenheit. This proves more than ample, as in practice, the reading has never exceeded 10 degrees above ambient.

In addition to heat buildup, high operating speeds can have a deleterious affect on rotor strain gage wiring . There is a significant amount of delicate wiring on the rotor. This wiring is secured with a combination of polyurethane adhesive, silicon RTV, and tape. At high speeds (3,000 RPM and up), centrifugal force is sufficient to cause wires and connectors to detach. A single wire coming off the rotor often pulls other wires off, and the final result is strain gages being pulled off the blades. As rotational speed increases, increasingly stringent precautions must be taken to prevent this.

2.1.2 Lubrication

Like any high speed rotating assembly, the spin pit requires proper lubrication. An oil mist is generated using a Norgren oil mister, and channeled through a series of intricate passageways to lubrication points near the bearings. Additional passageways function as reclassifiers, turning the fine oil mist into larger droplets suitable for lubrication, and depositing the droplets onto the bearings. An auxiliary oil conduit directs mist to the lower face seal housing area, ensuring a constant supply of lubricating and sealing oil to the face seal. Using standard oil requirements for bearing size, type, and operating parameters, the spin pit design calls for 15 PSI on the oil mister, and a flow rate of approximately 30 droplets per minute. These parameters are constantly monitored throughout spin pit operation.

2.1.3 Slip Ring

Since strain gages are mounted on the rotating rotor, a slip ring must be employed to transfer the strain gage signals. The slip ring consists of a series rotating of rings, mechanically connected to the rotor, which carry up to 25 independent signals. Brushes allow the rings to rotate freely while conducting the signals from the ring. The electro-mechanical interface between the brush and the ring introduces a small amount of synchronous electrical noise into the signal path due to small mechanical imperfections in the ring and brush assemblies (for further details, see [3]).

2.1.4 Excitation Magnets

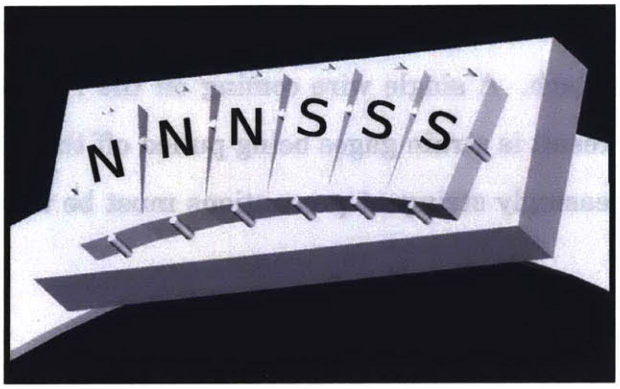

Figure 2-2: Excitation magnet module.

The turbine blades are excited using 18 powerful Cobalt Samarium magnets. They are rated at 9,850 Gauss and 8,750 Oersteds. The magnets are configured in three modules, each containing six individual magnets. They are arranged so that the polarity reverses in the center of each magnet module (Figure 2-2). This results in a rapid change in flux when a blade passes over the center of the magnet module. As per Lenz's Law[1], this generates a current in the blade, along with a corresponding magnetic field opposite that of the magnets [6]. The opposing magnetic field applies a force to the blade.

2.2 Test Articles

Two different rotors have undergone characterization and testing. The first rotor, shown in Figure 2-3, consists of three removable aluminum blades attached to a central hub. The blades are are based on the design of the GE90 Fan-C rotor blades. For fabrication and experimentation purposes, the GE design was modified to remove all twist and camber from the blade. The second test article, the Rocketdyne Mk3 blisk (Figure 2-3), comes from the turbopump of an RS-27 rocket engine. This rotor has 109 small blades constructed of Stellite-21, an extremely hard and heat resistant non-ferrous alloy. The blade tips have interlocking tongues, designed to dampen blade vibrations.

---

[1] "An induced electromotive force generates a current that induces a counter magnetic field that opposes the magnetic field generating the current."

Figure 2-3: Three-bladed rotor (left) and Mk3 blisk (right). Strain gages, bridge completion resistors, and wiring hub visible on both rotors.

2.3 Sensors

2.3.1 Magnetic Sensors

Inside the spin-pit, the ECS and VRS sensors are mounted on traverses overlooking the blade tips (Figure 2-5). Signals from these sensors pass through a vacuum seal to the outside of the spin pit. From there, the signals are passed through a conditioning amplifier and a common-mode rejection amplifier. Finally, the signals terminate in the data acquisition system.

ECS Sensors

ECS sensors are active type sensors, consisting of a coil driven by a high frequency oscillator [7]. This generates a time-varying magnetic field. When the field encounters a conductor, it induces eddy currents within the material [8]. The eddy currents in turn generate their own magnetic fields, which interact with the sensor coil. These field interactions manifest themselves as changes in the reactance of the sensor coil [9]. A special circuit measures the change in reactance of the coil, and converts it to a voltage that is proportional to the distance of the conductor from the sensor. Although material properties affect sensor performance, ECS sensors are generally

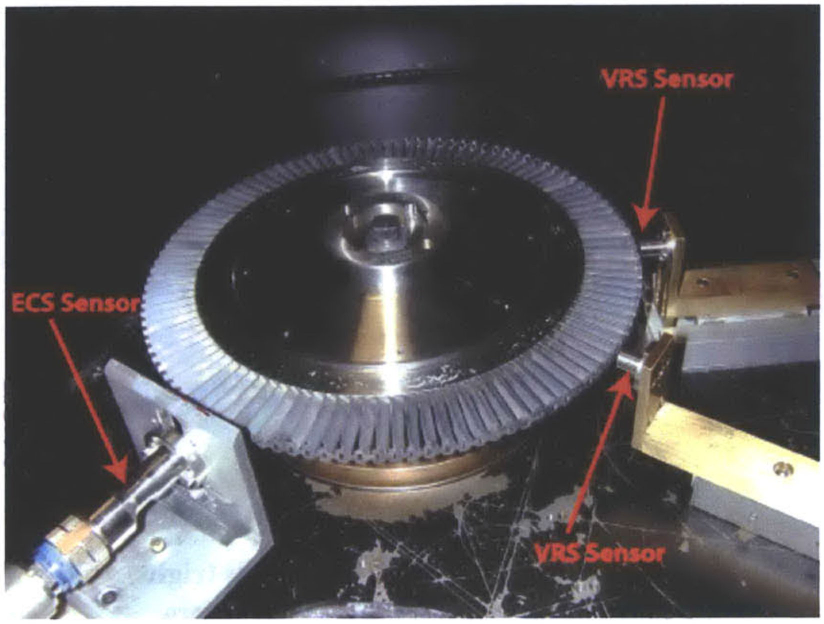

Figure 2-4: Picture of Mk3 blisk in spin pit, ECS and VRS sensors visible.

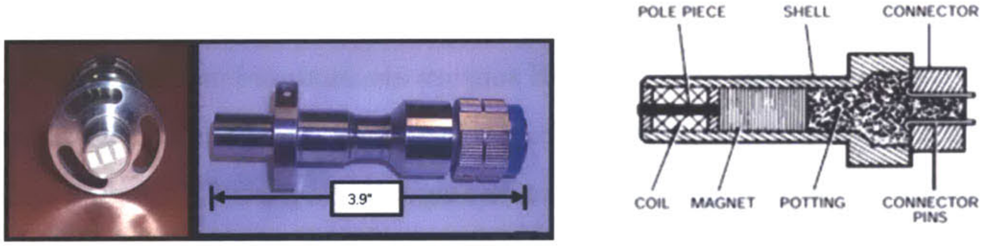

Figure 2-5: ECS sensor [1] (left) and VRS sensor [2] (right).

compatible with all good conductors.

The General Dynamics GDAIS (General Dynamics Advanced Information Systems) ECS sensor was used for this research. This ECS sensor is designed specifically for use in turbine engines, and is therefore ruggedized and heat resistant [10]. It consists of two field generation coils, and a single sensing coil [5]. This allows the sensor to produce a zero crossing when the blade passes through the sensor midpoint. The zero crossing point can be used to determine time of arrival, in addition to providing a reference point for further processing of the ECS pulse.

VRS Sensors

VRS sensors differ from ECS sensors in that they are a passive type of sensor. VRS sensors consist of a sensing coil wrapped around a central pole piece, and use permanent magnets to produce a static magnetic field which envelopes the coil [11]. When a ferrous material passes through the static field, it causes a change in reluctance (magnetic resistance), resulting in a change in the magnetic field [2]. The changing magnetic field induces a current in the sensing coil proportional to the rate of change [11]. This current can be directly measured with a volt meter.

VRS sensors are simpler and cheaper than ECS sensors since they do not require an oscillator and complex sensing circuits. Like ECS sensors, they produce a pulse with a zero crossing point that occurs when the blade passes through the sensor midpoint. However, VRS sensors only detect ferrous metals [2]. This makes them unsuitable for use with turbines made from non-ferrous alloys, or alloys that are only slightly ferrous. Another distinguishing characteristic of the VRS sensor is that its signal magnitude is a function of the rate at which the blade passes the sensor [11]. This contrasts with the ECS sensor, whose output is independent of speed.

2.3.2 Strain Gages

In addition to ECS and VRS sensors, strain gages are installed on the rotor itself. The strain gages provide a complete picture of the actual behavior of the blades. The signal from the strain gages is passed through a central hub to a slipring, which provides an electrical interface to the spinning rotor. These signals are then passed through strain gage conditioning amplifiers, and then into the data acquisition system.

Bridge Configuration

Strain gages change resistance in proportion to flexing of the test article on which they are mounted. To measure this change in resistance, the gages are wired in a Wheatstone Bridge configuration. Excitation voltage is applied to two opposing

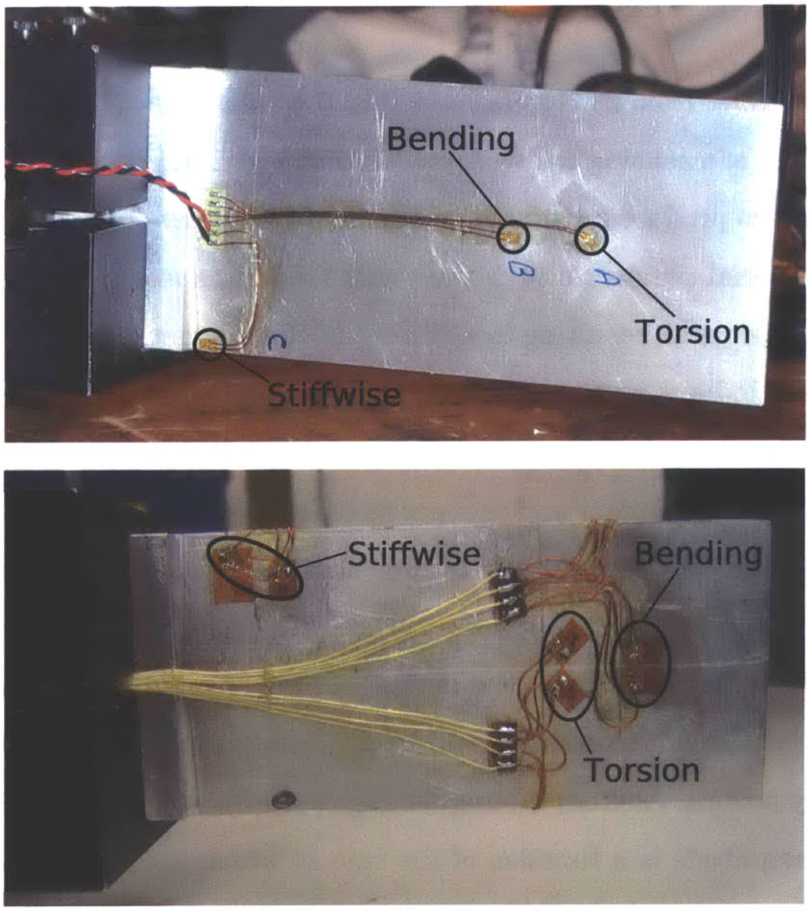

Figure 2-6: Quarter bridge strain gage setup (top), full bridge strain gage setup (bottom).

legs of the bridge, and voltage measurements are taken at the remaining two legs. Voltage is proportional to strain.

A number of different bridge configurations were used throughout the course of this research. The most sensitive configuration employed four strain gages [12], each corresponding to a resistor in the network. This is known as the "full bridge" configuration (Figure 2-6-bottom), and is the most time consuming to setup. The next most sensitive configuration used was the half-bridge [12], consisting of two strain gages and two bridge completion resistors mounted off-rotor. Finally, a single strain gage with three completion resistors was also used (Figure 2-6-top). This configuration, although least sensitive [12], was attractive because it only required installation of a single strain gage on the blade. For the Rocketdyne Mk3 blisk, this was the only option, as the blades were too small to accommodate additional strain gages (Figure

2-3-right).

Since small changes in resistance correspond to large fluctuations in strain, it is crucial that the bridge completion resistors be heat stabilized and of very high precision. Bridge completion was initially attempted using standard 2% resistor arrays, however wild fluctuations in strain were noted and believed to be the result of thermal instability. Eventually, purpose built, stabilized 0.025% resistors were installed with good results. To minimize slipring induced electro-mechanical noise, it is important that the bridge be completed on the rotor, before the strain signals pass through the slip ring.

Calibration

Calibration of the strain measurement system establishes the mapping between strain gage amplifier output in volts and actual strain, measured in units of microstrain [12]. First, a conversion factor must be chosen. In general, this factor should be small enough to provide good resolution, but large enough to avoid clipping in the amplifier output. Once the conversion factor is chosen, a shunt resistance can be calculated. This shunt resistance is applied across one of the strain gages in the bridge, simulating a strain in the strain gage, and the amplifier gain adjusted for maximum output [3].

All data in this research were collected using a conversion factor of $520\mu\epsilon/V$. Although the strains encountered allow for a lower, and therefore higher resolution, conversion factor, this value corresponds to the maximum resistance (11,999Ω) of the "decade box" used in the shunt. Higher strain data quality could be achieved with a more capable decade box [3].

2.3.3 Vibration Sensor

An accelerometer is mounted directly to the bearing housing of the spin pit, and is connected to a Bruel-Kajear "Nexus" conditioning amplifier. It is used to measure vibration of the running spin pit. Vibration measurement is critical to in-situ balancing of the rotor. Using a technique detailed in Yiben Lin's work [13], vibration measurements are taken with a test mass placed at various points on the rotor. A geometric relationship can then be used to determine the mass and position of a balancing weight.

2.4 Data Acquisition

Given the myriad of sensors, a multichannel data acquisition system is required. The National Instruments NI-6071E is the instrument of choice. It is a 16-channel, 12-bit, 1.25Hz maximum scan rate DAQ. Scanning is sequential, which means that each channel is phase shifted $\frac{1}{f_{sample}}$ seconds from its neighbor (see Section 4.3.1). The maximum sample rate per channel is a function of the number of channels desired, $\frac{1.25 \cdot 10^6}{N_{channels}}$ samples per second. The DAQ is controlled and configured using the LabView graphical environment.

Chapter 3

Data Collection

To develop and test algorithms for vibration detection, large quantities of empirical data are required. There are two primary types of data. The first is hammer test data, which is used for determining the natural frequencies of a test article. These frequencies determine the speed parameters used in subsequent spin testing.

The second data type is spin pit data. This consists of tachometer, strain, VRS, and ECS data taken while spinning a rotor in the spin pit. Data were collected using two different test articles, the experimental three-bladed rotor, and the Rocketdyne Mk3 turbopump blisk. Most data sets were taken in matching pairs, with a test first conducted without magnetic excitation, and then duplicated with the excitation.

3.1 Hammer Testing

Knowledge of blade natural frequencies is critical when planning a data collection run. The natural frequencies are ascertained by hammer testing. This involves tapping the test article with an instrumented hammer, and recording the blade response. The hammer contains an accelerometer, which records the impact of the hammer head on the blade. Data from the blade can be collected using two different types of sensors. The first is a small accelerometer, which is secured to the blade using an adhesive wax compound. The other sensor type is the strain gages, which are permanently glued to the blade.

The data are collected using an HP 35665A spectrum analyzer. The analyzer is set to trigger on the signal from the hammer accelerometer, and to collect blade vibration data on the other channel. Uncorrelated noise is accounted for by averaging the results of 50 to 100 hammer taps. Initial hammer test data were taken using the accelerometer. The accelerometer weighs approximately 1g. It was hypothesized that this extra mass on the blade could affect the measured natural frequency. To test this, hammer testing was done on the same article first using the accelerometer, and then the strain gages. The results indicate that one of the modes shifts down in frequency by approximately 200Hz (Figure 3-5). Therefore all subsequent hammer test data were collected with the strain gages. This has the added advantage of taking hammer data from the blade in exactly the same configuration used for spin testing (i.e. the strain gages are on the blade in the spin pit and the accelerometer is not).

3.1.1 Three-bladed rotor

Hammer testing was conducted on the three-bladed rotor for three mode shapes: bending, torsion, and stiffwise bending (Figure 3-1). The bending mode was excited by tapping the blade mid-chord at the tip, torsion was excited by tapping the blade at an edge of the tip, and stiffwise excited by tapping the blade at the tip in the stiffwise direction.

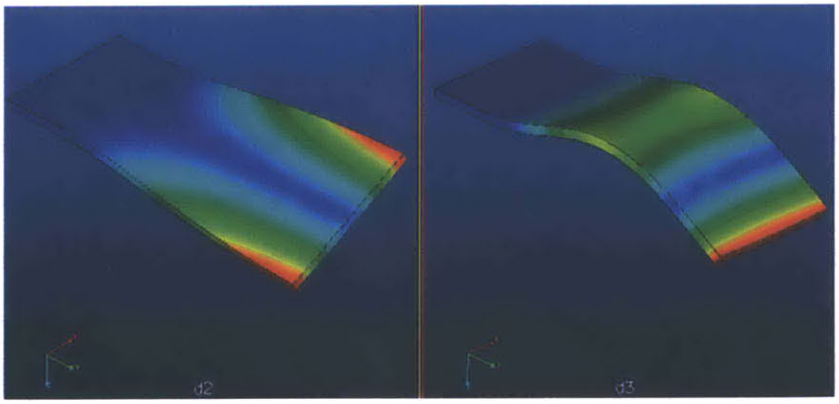

Figure 3-1: Simulation of first torsion (left) and second bending (right) modes using flat plate blade model [3].

Table 3.1: Three-bladed rotor mode frequencies.

Mode	*MIT Testing Frequency (Hz)*	*Pratt Testing Frequency (Hz)*	*Discrepancy*
1^{st} Bending	358.2	357.8	−0.11%
1^{st} Torsion	1222	1273	+4.17%
2^{nd} Bending	1294	1333	+3.01%
2^{nd} Torsion	2989	3127	+4.62%
3^{rd} Bending	3109	3261	+4.89%

Initial tests were conducted using the accelerometer, which was placed on the blade according to the mode shape of interest. Subsequent testing was done with the on-blade strain gages. Table 3.1 sums up the results, illustrated in Figure 3-2. There are some discrepancies between testing conducted by MIT and Pratt & Whitney. This can be attributed to a number of factors. First, since two different blades of identical design and material were used by MIT and Pratt, manufacturing differences may have slightly influenced the results. Moreover, Pratt mounted their blade on a broach block and excited it using an audio speaker. Pratt's measurements were taken with a laser vibrometer, which is a non-contacting device that measures Doppler shift from a reflected laser beam, whereas MIT testing was conducted with on-board strain gages. Nevertheless, the agreement in Table 3.1 is reasonable and sufficient for the purposes of this research.

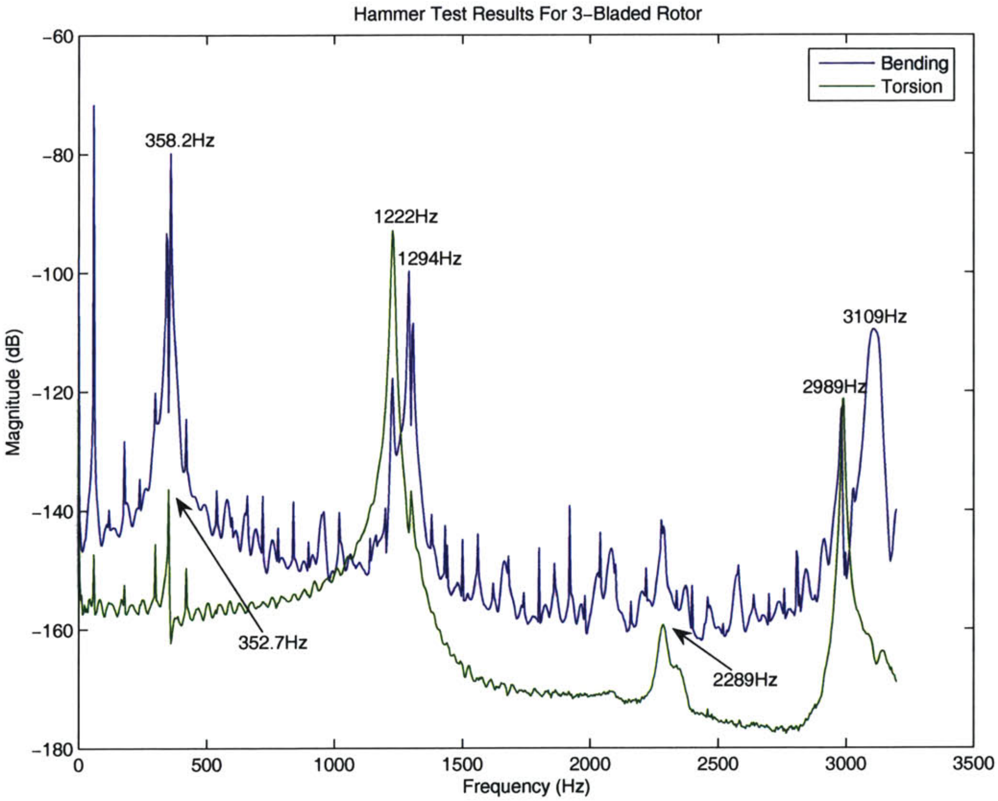

Figure 3-2: Hammer test results for three-bladed rotor.

Mode Shape Identification

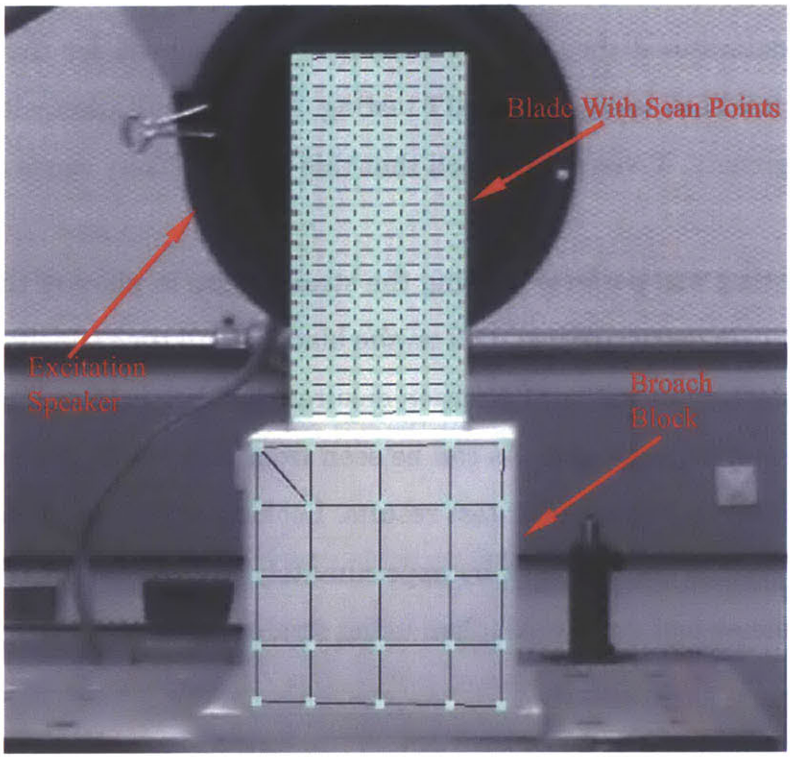

Figure 3-3: Vibrometer test setup (courtesy of Pratt & Whitney).

Using the analysis done by Pratt & Whitney as a basis, it is possible to infer the mode shape of each natural frequency (Appendix B). The laser vibrometer provides mode shape information directly. This is achieved by rapidly scanning the vibrometer beam over the area of the blade and recording displacement as indicated by Doppler shift. A pictorial representation of displacement can then be achieved by overlaying this data as a color map on top of the test article (Figure 3-3).

3.1.2 Mk3 Blisk

Unlike the three-bladed rotor, the MK3 blisk has only one strain gage installed per blade, in the bending direction. This is necessitated by the significantly smaller blades of the blisk. Hammer testing was initially conducted using the accelerometer. However, the results were inconsistent with Rocketdyne's hammer test data. Comparing plots in Figure 3-4, it is evident that there is virtually no overlap between the mode peaks of the two test runs. Additional tests were performed, and all were consistent and did not match the Rocketdyne results. After discussing the discrepancy with Rocketdyne, it was determined they had been using a quarter blisk for their testing, in contrast to the full blisk used for the MIT testing. After consultation with Rocketdyne structural engineers, it was determined that this was the likely cause of the discrepancy.

Additional hammer testing was performed using the strain gages in place of the accelerometer. Since the strain gages are installed on the blades at all times, including during runs, hammer testing in this configuration ensures the blisk is in exactly the same state as when a run is performed. As can be seen from Figure 3-5, the accelerometer did have an effect on the hammer test results. Looking at the cut blade, for example, the 4300Hz mode is shifted down by approximately 200Hz. As a result of this, all subsequent hammer test data were taken using strain gages.

3.2 Spin Test Plans

Without a well designed test plan, data collection is a random, haphazard exercise. The first step in developing a test plan is to clearly layout the purpose of the test, the algorithms to be applied to the data, and the equipment limitations. Next, hammer testing of the article must be conducted. Hammer testing identifies the natural frequencies of the test article. All spin pit testing is generally centered around rotational speeds F_r that are harmonics of these natural frequencies F_m:

$$F_r = \frac{F_m}{3n} \tag{3.1}$$

where n is a positive integer.[1] Once these factors are taken into account, a detailed test plan can be compiled. An example of such a plan, for the three-bladed rotor, is illustrated in Appendix A.

---

[1] Multiple of three harmonics are expected to generate the greatest response since there are three magnet modules in the spin pit.

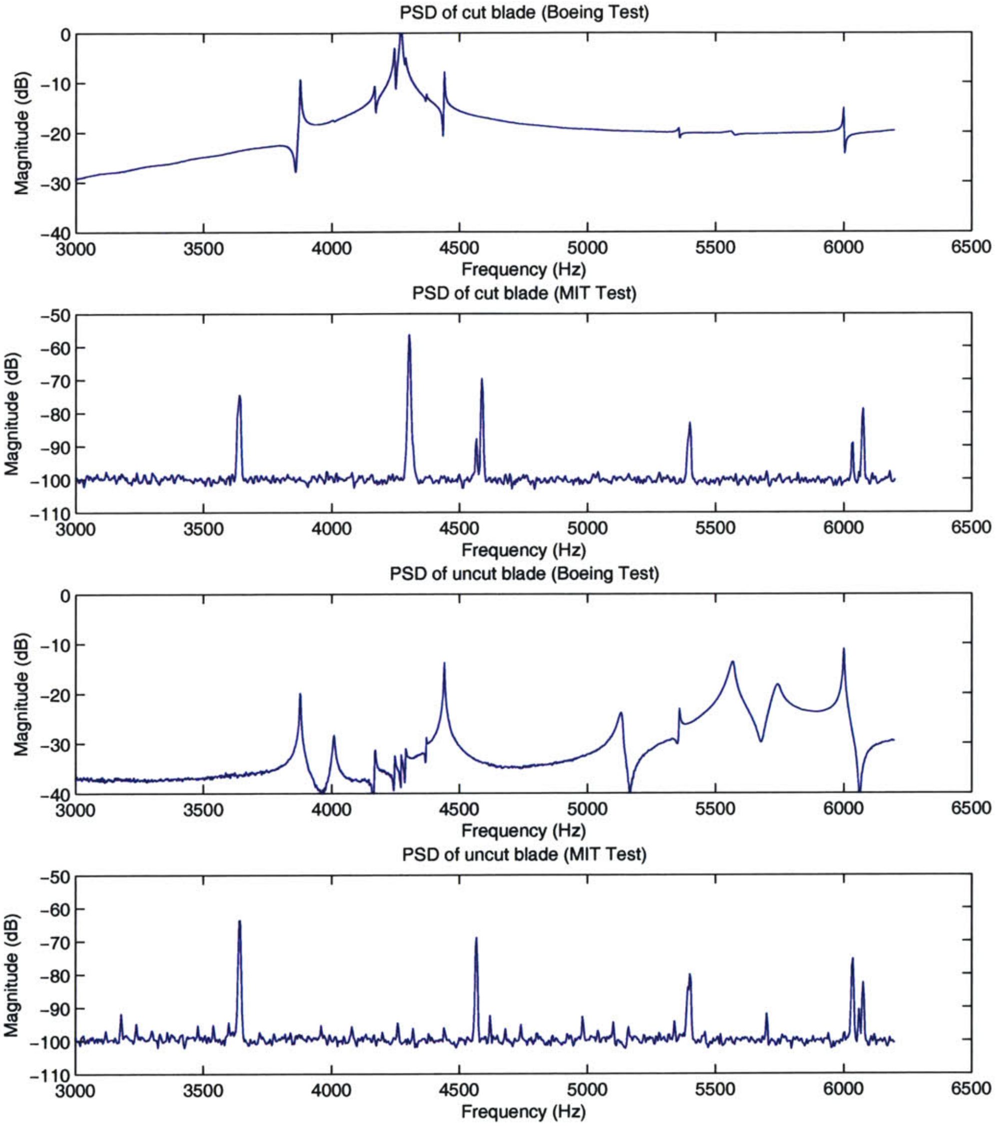

PSD of cut blade (Boeing Test)

PSD of cut blade (MIT Test)

PSD of uncut blade (Boeing Test)

PSD of uncut blade (MIT Test)

Figure 3-4: MIT vs. Rocketdyne hammer tests.

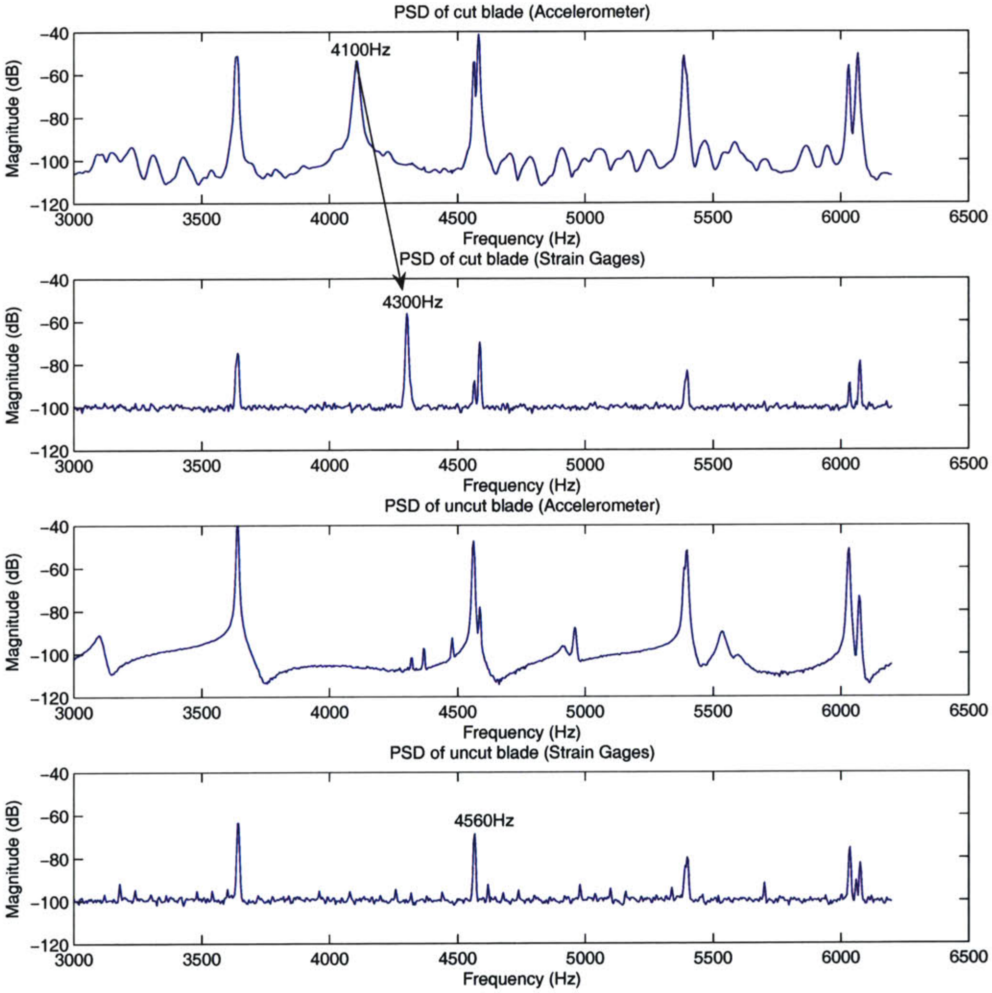

Figure 3-5: Accelerometer vs. strain gage hammer test results.

Table 3.2: Data type designators.

Suffix	*Description*
ot	Order Tracking Data
ecs	ECS Data
lv_s<sample rate>	LabView Data (raw strain gage, ECS, and tach)

3.2.1 Data File Naming Scheme

Since the spin pit generates large quantities of data across disparate data collection systems, a well organized system is needed to keep track of the data. Towards this end, a file naming specification was developed. Encoded in the file name for each set of data is the blade number, test number, run number, data type, and sample rate. These values are taken directly from the test plan.

Files are named using the following format:

b<blade number>t<test number>r<run number>_<data type>

Take the data file "b1t02r04_lv_s100" as an example of this naming scheme. Using Table A.1, the first part of the file name decodes to "blade 1 test 2 run 4" and from Table 3.2 this file contains LabView data taken at a 100KHz sample rate. Column layout for each data file is defined in a text file located in the data directory. The columns are defined in a colon delineated list.

3.2.2 Run Profiles

Determining the appropriate speed profile for a run is a critical element in the planning process. In general, three different profiles were used, the ramp, the step, and constant speed (Figure 3-6). The ramp is advantageous for finding speeds of high response and for collecting data over a wide range of speeds. However, the ramp must be slow enough so as to allow sufficient time to elapse to collect data at a specific speed [14]. This ramp rate is defined by an ISO standard [14] as:

$$R_{sweep} < 216(f_l)^2(\zeta_r)^2 Hz/min \tag{3.2}$$

where R_{sweep} is the maximum sweep rate in Hertz per minute, f_l is the lowest frequency mode, and ζ_r is the damping coefficient.

Additionally, the tachometer is only a once per revolution pulse. This coarse measurement means each rotor speed data point is the average speed of one full revolution. To determine inter-revolution speed, extrapolation from the ramp rate is necessary.

3.2.3 Minimum Sample Rates

The three different sensor types each have different minimum sample rate requirements. The strain gages are the easiest to account for, since they reside on the blade itself and are therefore only subject to the Nyquist Criteria of $f_s = 2 * f_{max}$. Strain gage sample rates can thus be deduced from the mode frequencies found in hammer testing. The appropriate sample rate is simply twice the mode frequency of interest [15]. In practice, this rate was itself doubled to account for any unexpected side effects of exciting the rotor in the spin pit.

Next, a sample rate for the VRS tachometer must be found. Since the sensor detects a small recess in the slipring shaft passing by once per revolution, the signal can be roughly modeled as a single cycle sine wave when the recess passes under the sensor, and zero elsewhere. The period of the sine wave component can be found by dividing the diameter of the recess D_r by the shaft circumference C_s multiplied by the shaft speed F_s

$$T_{tach} = \frac{D_r}{C_s F_s} \tag{3.3}$$

By the Nyquist Criteria, the minimum sample rate is then $\frac{2}{T_{tach}} Hz$:

$$f_s = \frac{2 C_s F_s}{D_r} \tag{3.4}$$

For unexcited runs (i.e. non-vibrating blades), the procedure for estimating the minimum sample rate for the ECS sensors is similar to that used for the tachometer.

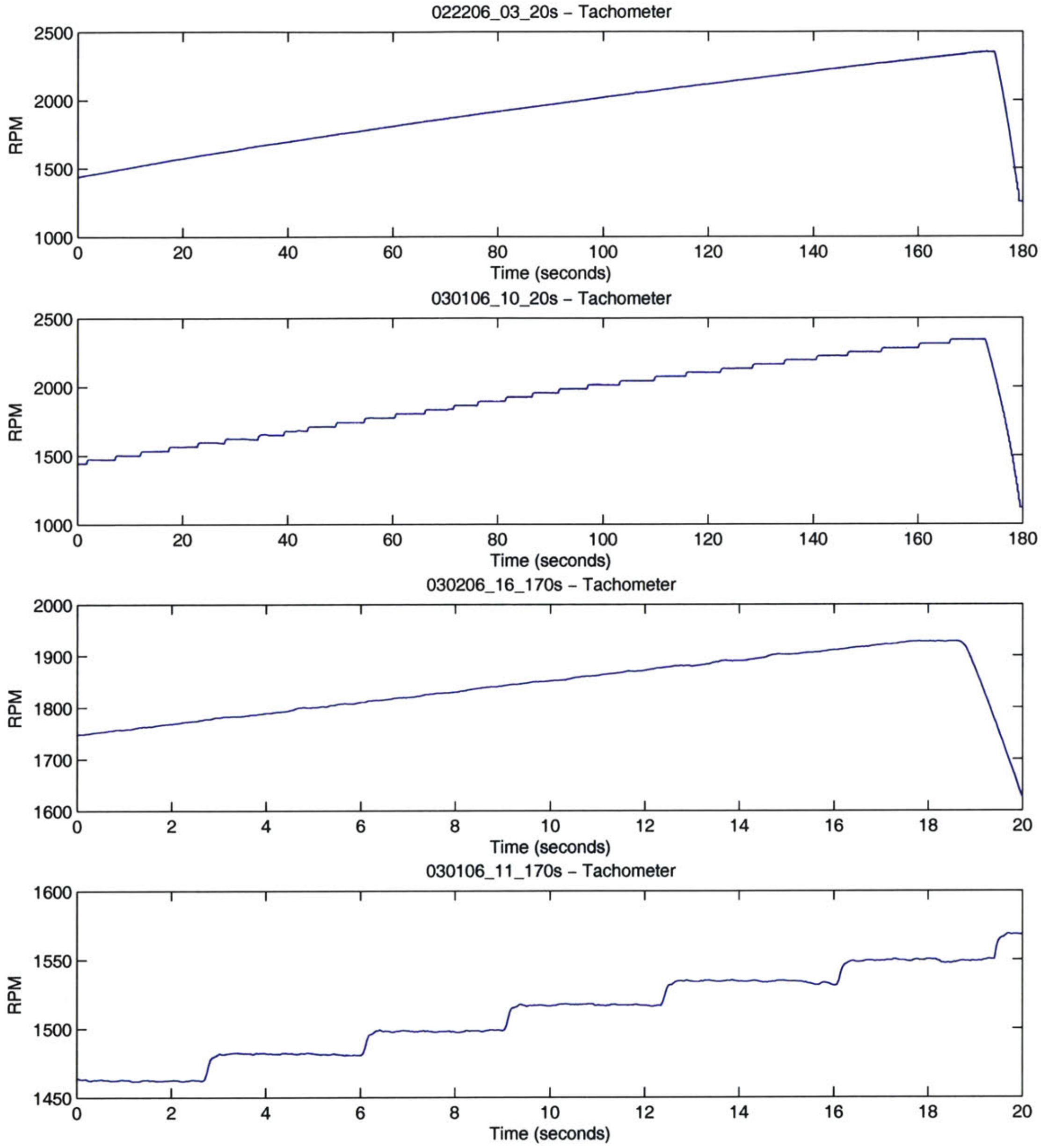

Figure 3-6: Example speed profiles. Fast ramp (top), fast step (second from top), slow ramp (second from bottom), and slow step (bottom).

The only difference is that the width of the sensor itself is used for D_r since the sensor is wider than the blade. The procedure must be modified for excited runs to take velocity due to blade vibration into account. To begin, blade tip deflection is modeled as a sine wave whose frequency F_m is the highest frequency mode of interest, and whose amplitude A corresponds to maximum tip deflection for that mode found from hammer testing:

$$d(t) = A\sin(2\pi F_m t) \tag{3.5}$$

The velocity function for the blade can be found by taking the first derivative of 3.5

$$v(t) = d'(t) = 2\pi A F_m \cos(2\pi F_m t) \tag{3.6}$$

Since the cosine function has a magnitude of 1, the maximum blade velocity due to excitation is simply $2\pi A F_m$. This can be converted into a rotational speed F_b in Hertz by dividing by rotor circumference C_r

$$F_b = \frac{2\pi A F_m}{C_r} \tag{3.7}$$

From this, an excitation corrected shaft speed is easily found:

$$F_{sb} = F_s + F_b \tag{3.8}$$

ECS pulse period is subsequently calculated using the same form as Equation 3.3

$$T_{ecs} = \frac{D_{ecs}}{C_r F_{sb}} = \frac{D_{ecs}}{C_r F_s + 2\pi A F_m} \tag{3.9}$$

where D_{ecs} is the diameter of the ECS sensor. Applying the Nyquist Criteria, the minimum ECS sample rate is thus $\frac{2}{T_{ecs}} Hz$:

$$f_s = \frac{2(C_r F_s + 2\pi A F_m)}{D_{ecs}} \tag{3.10}$$

It is important to note that all of these equations set only a lower bound for the sample rate. In practice, it is possible that there may be subtle features of the data that exhibit rise times which exceed those assumed, or which may fall between samples. Moreover, although sinc interpolation can in theory reproduce an arbitrary number of samples perfectly, implementation constraints such as numerical error and finite window length can introduce error into interpolated samples. Therefore, the highest feasible sample rate supported by the DAQ hardware was always used.

3.3 VRS Sensor Performance Testing

After analyzing multiple runs of Mk3 blisk data, it was observed that the signal from the VRS sensor was much lower than expected. The signal was so weak that it was almost impossible to discern the pitch signal from the passing of the 109 blisk blades. Inspection and testing of all of the equipment revealed no anomalies. It was thus hypothesized that there was an incompatibility between the blisk and the VRS sensor.

To test this hypothesis, a single stellite blade identical to those found on the blisk was passed in front of the VRS sensor. As indicated in Figure 3-7, no response was observed. Then, a 30 mil steel feeler gage was passed in front of the VRS sensor at the same speed and distance. A significant response was noted (Figure 3-7). It was thus concluded that the VRS sensor was not compatible with the stellite alloy. Further research indicated that VRS sensors only respond to ferrous materials [2]. The small response seen in the spin pit data was therefore attributed to the combination of high speed and the 3% iron content of the stellite alloy. Since both the Mk3 blisk and the three-bladed rotor are made from non-ferrous materials, the VRS sensor was eliminated from further data collection and judged unsuitable for this application.

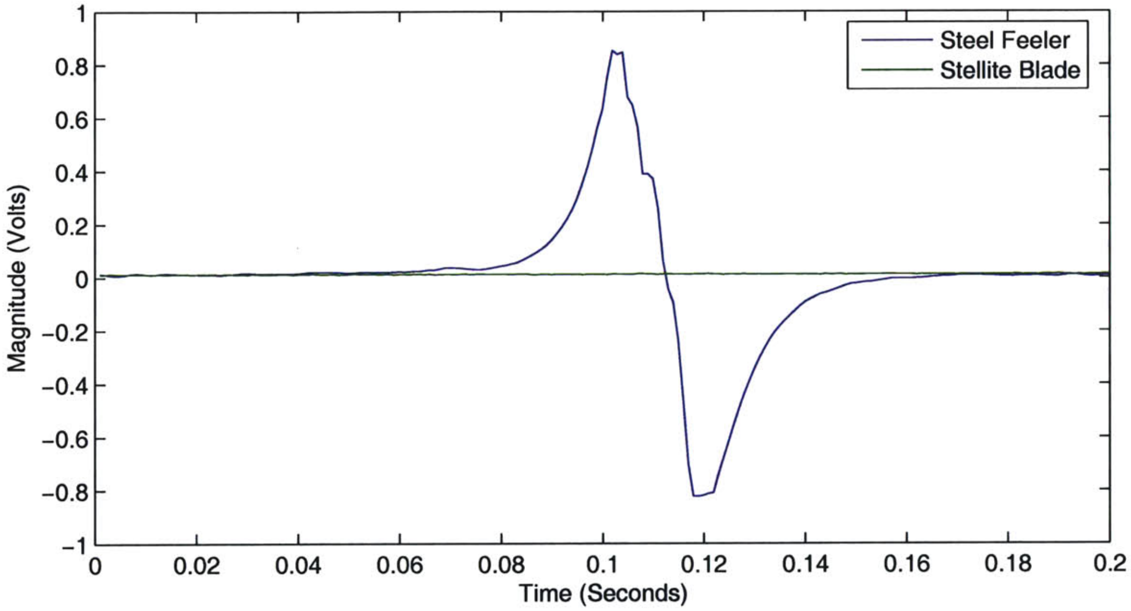

Figure 3-7: Comparison of VRS response to steel feeler gage versus stellite blade.

Chapter 4

Data Reduction

Each run of the spin pit produces in excess of 200MB of time-domain data. Clearly, it is not possible to infer much directly from such an immense quantity of data. A number of tools have therefore been developed to facilitate this process. First, a simple script was created to derive rotor speed from the tachometer pulse train. Then, code was developed to read the raw data files, and generate a series of spectrograms. The spectrograms are three-dimensional visualizations of frequency as a function of time, and serve to guide further data analysis.

Following spectrogram characterization, a number of algorithms were applied to the data. The first of these is based on the Hilbert transform, and produces instantaneous frequency and phase-plane data. A residue characterization algorithm was then applied, and its results compared to those of a model-based predictor. Lastly, the performance of an adaptive filter algorithm is examined.

4.1 Spectrograms

In order to understand blade characteristics and to evaluate the performance of a run, it is helpful to reduce large data sets into compact representations of critical parameters. In the case of a vibrating turbine blade, the most important quantities are frequency and magnitude of vibration. They can be derived from strain gage data using a short-time Fourier transform. Unlike the standard Fourier transform which is computed over an entire data set, the short-time Fourier transform is computed over a sequence of shifted finite length windows, introducing a time dependence in the equation [16]. This can be seen from the definition of the STFT:

$$X(n,\lambda) = \sum_{m=-\infty}^{\infty} x(n+m)w(m)e^{j\lambda m} \tag{4.1}$$

In 4.1, x is the signal of interest, in this case strain data, and w is a window function. Unlike the conventional Fourier transform, which is defined as a function of frequency alone, the STFT is a function of both frequency, n, and time, λ [16]. This allows one to see the evolution of frequency magnitude over time. Visually, this is represented as a spectrogram plot. The plot shows frequency on the x-axis and time on the y-axis. Frequency magnitude can be represented either as color in a two dimensional plot (Figure 4-1), or as the z-axis of a three dimensional contour. Since the strain data usually consist of many different frequencies distributed throughout the frequency band and throughout time, three dimensional contours contain many small peaks and valleys, making them difficult to interpret. The two dimensional plots are far more convenient.

4.1.1 Automated Spectrogram Generation

To facilitate the easy creation of spectrograms from raw data, a set of Matlab scripts was developed. These scripts read in a raw data file, process and plot the tachometer signal, and then compute spectrograms for each sensor. Spectrogram plots can either be manipulated interactively or automatically placed in a directory corresponding to the data file they were generated from. To prevent confusion, each spectrogram image file name includes the name of the raw data file from which it was generated. The ease of spectrogram generation makes it practical to do first order data analysis after each run. Subsequent run parameters can then be established or tuned based on the results of previous runs.

4.1.2 Spectrogram Interpretation

Each spectrogram represents an interpretation of the entire run for a particular sensor. Much useful information can be quickly gleaned from this. First, blade resonances are clearly evident by narrow-band dark red blotches (Figure 4-1), indicating relatively large magnitude response. These high magnitude areas of vibration should correspond to the modes previously identified during hammer testing. In this case, comparing to Figure 3-2, we see that the response matches up to the 1294Hz mode. The diagonal lines of medium response corresponds to integral multiples of shaft speed. As time, and therefore shaft speed, increases, so too does the frequency of these bands. The time of the most significant vibrations can be noted on the spectrogram and cross-referenced with the tachometer data, which indicates rotor speed as a function of time, to determine the rotor speed over which the vibration occurred. Spectrograms also clearly show motor and electro-mechanical noise.

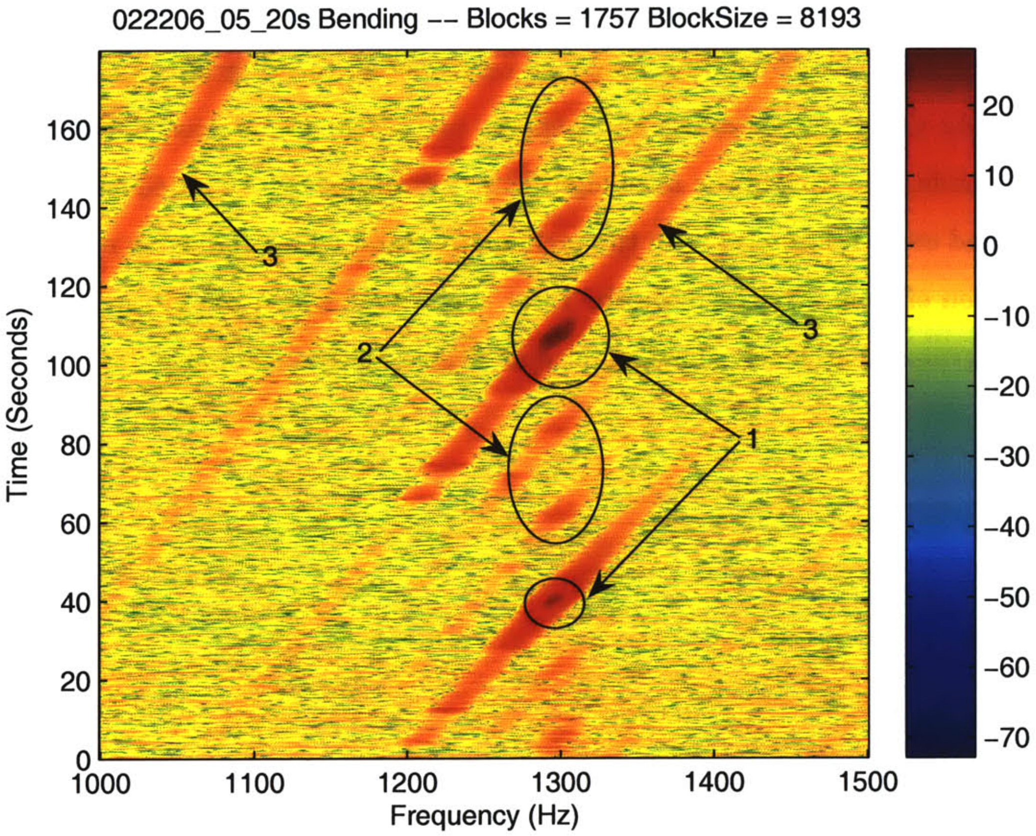

Figure 4-1: Typical spectrogram showing **1**–major modes at shaft speed multiples of 3, **2**–minor modes at integral speeds not a multiple of 3, and **3**–synchronous vibrations at non-resonant frequencies.

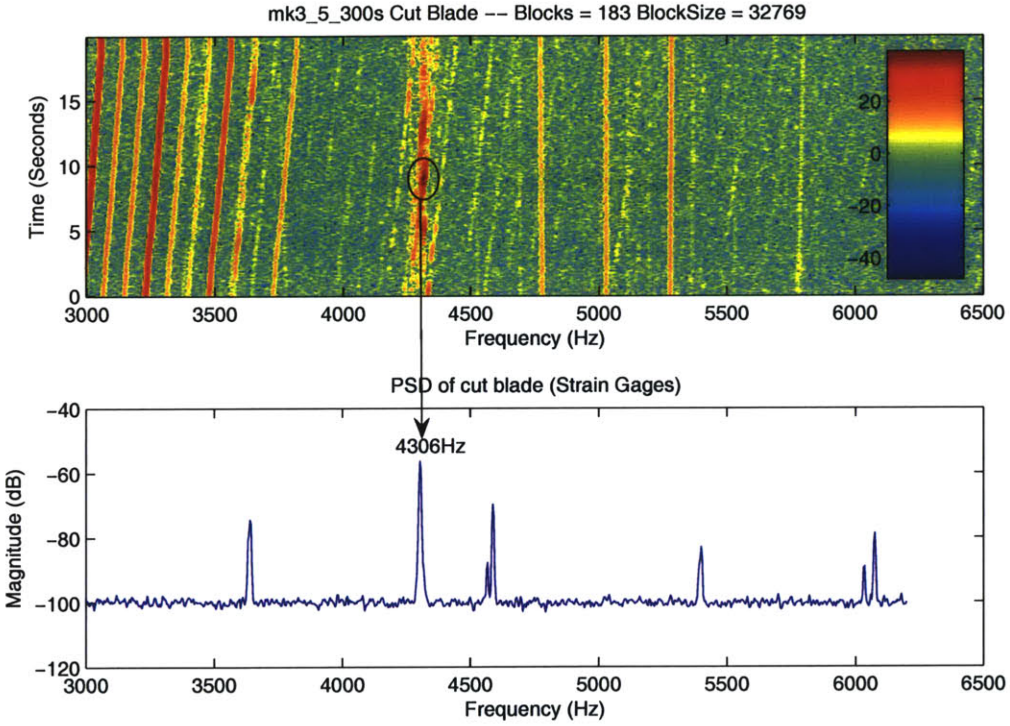

Figure 4-2: Mk3 blisk spectrogram (top) and hammer test results (bottom).

4.2 Hilbert Transform Methods

The Hilbert Transform is a special class of transform that phase shifts a signal 90 degrees for all frequencies. In time, this is achieved by a convolving the data $v(t)$ with 1/t [17]:

$$v_h(t) = v(t) * \frac{1}{\pi t} = \frac{1}{\pi} PV \int_{-\infty}^{\infty} \frac{v(\tau)}{t-\tau} d\tau \tag{4.2}$$

and in the frequency domain [17]:

$$\mathcal{V}_{\mathcal{H}}(\omega) = -j \cdot Sign(\omega) \cdot \mathcal{V}(\omega) \quad = \begin{cases} j\mathcal{V}(\omega) & \text{for } \omega < 0, \\ 0 & \text{for } \omega = 0, \\ -j\mathcal{V}(\omega) & \text{for } \omega > 0. \end{cases} \tag{4.3}$$

The transform is most easily understood by examining the frequency domain representation. By 4.3, we see that the Hilbert Transform of $\mathcal{V}(\omega)$ in the frequency domain is merely $j\mathcal{V}(\omega)$ on the left hand side and $-j\mathcal{V}(\omega)$ on the right hand side. A one-sided frequency domain representation can be constructed:

$$\mathcal{V}_{\mathcal{A}}(\omega) = \mathcal{V}(\omega) + j\mathcal{V}_{\mathcal{H}}(\omega) \tag{4.4}$$

$\mathcal{V}_{\mathcal{A}}(\omega)$ now consists of zero for the left hand side ($\omega < 0$), and $2\mathcal{V}(\omega)$ for the right hand side ($\omega > 0$). Taking the inverse Fourier transform results in the analytic signal representation:

$$v_a(t) = v(t) + jv_h(t) \tag{4.5}$$

The analytic signal $v_a(t)$ is complex valued and has no negative frequency components. It contains the same amount of information as the original signal $v(t)$ since knowing one side of a Fourier transform allows one to construct the other [18]. Note that $\mathrm{Re}\{v_a(t)\}$ returns the original signal, and $\mathrm{Im}\{v_a(t)\}$ returns the Hilbert transform of the signal. The analytic signal is convenient because the instantaneous frequency of the analytic signal is directly related to the derivative of its phase [19].

4.2.1 Instantaneous Frequency

Consider a phasor in the complex plane whose coordinates on the real axis are given by $\mathrm{Re}\{v_a(t)\}$, and whose coordinates on the imaginary axis are given by $\mathrm{Im}\{v_a(t)\}$. As time increases, the phasor rotates and forms a phase angle ϕ with the real axis. The rate of change of this phase angle determines the instantaneous frequency [19]:

$$\omega_i(t) = \frac{d\phi(t)}{dt} = \frac{d}{dt}\tan^{-1}\left(\frac{\mathrm{Im}\{v_a(t)\}}{\mathrm{Re}\{v_a(t)\}}\right) \tag{4.6}$$

Since the instantaneous frequency is a scalar value at a particular time, it can only represent one particular value at a time. When more than one frequency is present in a signal, the value of the instantaneous frequency at that point in time is approximately a weighted average of the frequencies present at that time.[1]

Properties of the Instantaneous Frequency

The concept of instantaneous frequency is counterintuitive at first glance, since in discrete time frequency is defined over a finite time interval. The concept becomes clearer by combining the analytic signal definition (Equation 4.5) with the definition of instantaneous frequency in 4.6 to find:

$$\omega_i(t) = \frac{d}{dt}\tan^{-1}\left(\frac{v_h(t)}{v(t)}\right) \tag{4.7}$$

Equation 4.7 helps to illustrate a number of properties of the instantaneous frequency. First, the numerator of the $\tan^{-1}$ argument is the Hilbert transform of the signal. From definition of the Hilbert transform in 4.2, it is evident that the Hilbert transform is a global operation. The value of the Hilbert transform at any point in time is found by convolving over all time. The instantaneous frequency is thus dependent on the data over all time. However, the denominator of 4.7 depends only on

---

[1] This assumes the signal is relatively steady-state.

the value of the data at time t, making the denominator a local property. Equation 4.7 is therefore both globally and locally dependent on the data.

Equation 4.7 shows that finding the instantaneous frequency requires taking the derivative of the arc tangent function. This derivative is highly non-linear, and is largest around the origin. Consequently, when the numerator of the argument to the arc tangent is small, such as around the left and right edges of of an ECS pulse, the instantaneous frequency is extremely sensitive to small magnitude transient noise in the denominator. Since the denominator depends only on the the data at a single point in time, even a single sample transient can lead to large fluctuations in instantaneous frequency.

4.2.2 Instantaneous Frequency For Blade Vibration

Based on the work of Teolis et. al. [1], the Hilbert Transform was explored as a means of detecting blade vibration using ECS sensors. A number of Matlab scripts were developed to process the data and plot the instantaneous frequency (Figure 4-3) and the phase-plane representation (Figure 4-4) for each ECS cycle (Figure 4-5).

The Hilbert transform method proved to be unworkable for deriving blade vibration parameters. The subtle blade vibrations are averaged out by the large magnitude pitch signal and the noise signal. This method may be useful if the noise and pitch signals could be eliminated via filtering. One possible method is the Empirical Mode Decomposition (EMD). This technique allows multicomponent signals to be broken down into monocomponent signals more suitable for processing with the Hilbert transform [20].

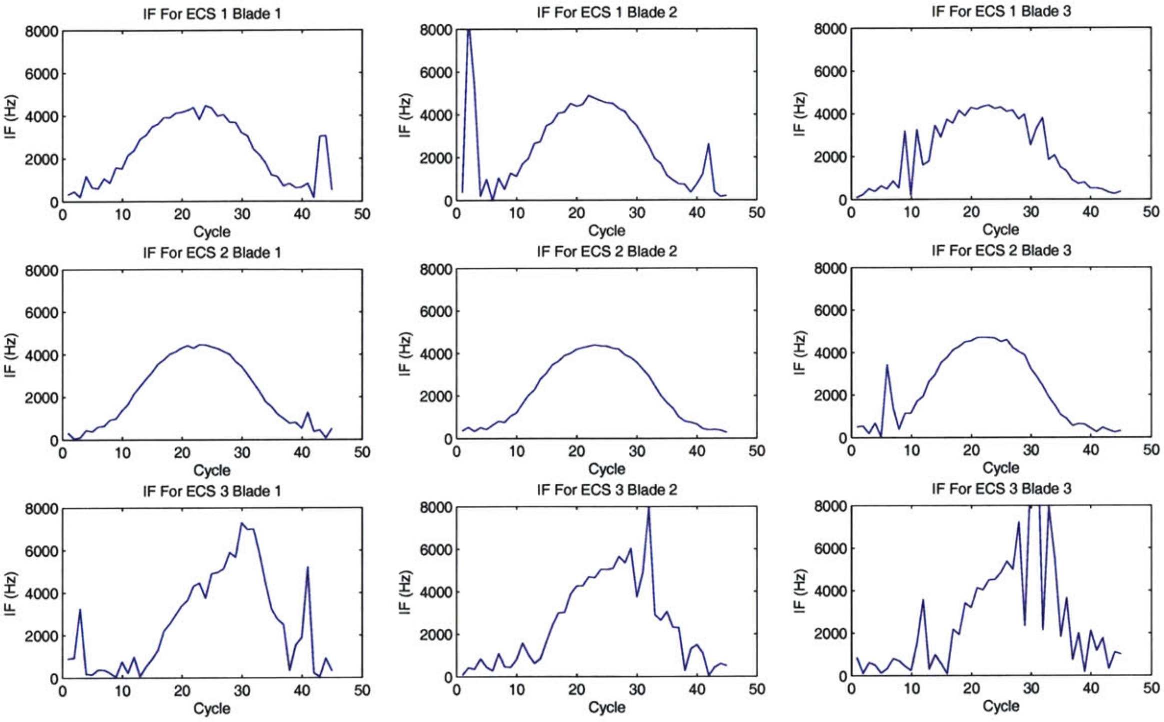

Figure 4-3: Instantaneous frequency plots for cycle 408.

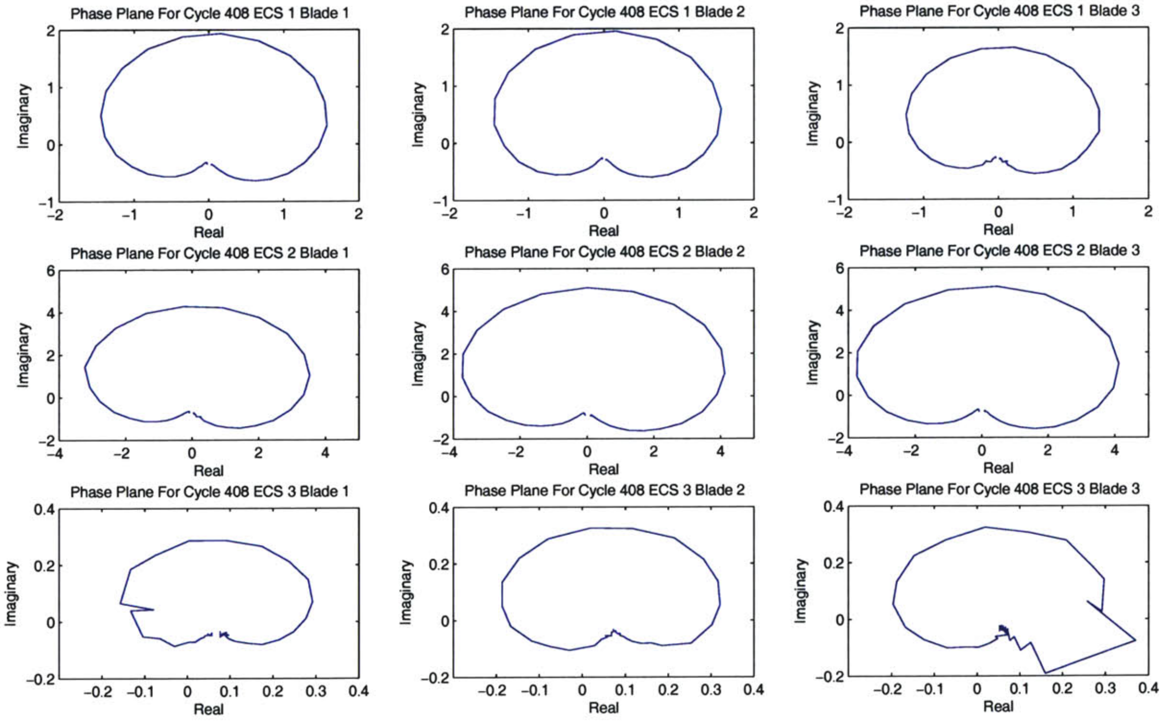

Figure 4-4: Phase plane plot of Hilbert transform.

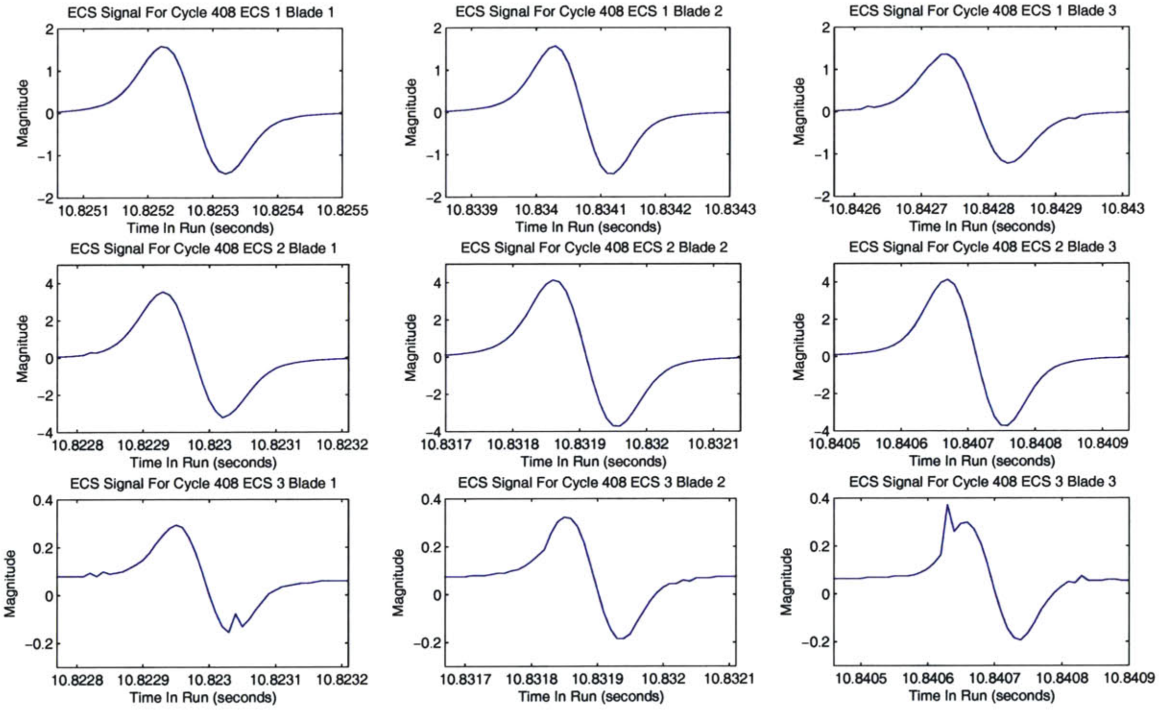

Figure 4-5: ECS waveforms for cycle 408.

4.3 Residue Characterization Methods

Unlike the previous methods, residue characterization methods do not involve radical filtering or transformation of the data. Rather, data are compared directly with one another, after accounting for shaft speed differences and noise. The result of the comparison is a residue, which shows the differences between the baseline ECS signal and the processed signal of interest. To make sense of the residues, two related simulation methods were developed. The first method models the expected residues resulting from four independent components: tip clearance, arrival time, velocity, and acceleration. The second method unifies the components to simulate real-world residues.

4.3.1 Algorithm Outline

To facilitate a basic understanding of the data processing algorithm, a high-level outline is presented. This is followed by more detailed description.

Algorithm outline for processing baseline data:

1. Filter tachometer signal and find zero-crossing points.
2. Window all data channels between desired pair of tachometer zero-crossing points.
3. Subsample shift all data channels to correct for DAQ scanning phase shift.
4. Find ECS signal zero-crossing points.
5. Window desired ECS pulse around zero-crossing point.
6. Window all other data channels around this point.
7. Upsample and sinc interpolate all windowed data.
8. Recompute zero-crossings for tachometer and ECS signals.
9. Subsample shift ECS data so zero-crossing point falls on integer sample.

Tachometer Filtering and Windowing

The tachometer is the reference pulse used to frame all data for each revolution of the rotor. A single revolution is defined as the time between zero crossings of two adjacent tachometer pulses. A reliable means of finding zero crossing points is thus required. By observing that the tachometer pulse only crosses zero when its derivative is large and positive, and that by definition there must be a sign change at the zero crossing point, the method for finding the zero crossing becomes obvious. The algorithm simply searches the tachometer signal for points of positive derivative and then searches within those points for a sign change across adjacent samples. The first sample before the sign change is returned. To find the actual zero crossing point, linear interpolation is carried out, shown graphically in Figure 4-6-bottom.

This simple algorithm is adversely affected by noise. As illustrated in Figure 4-6-

top, there is significant low magnitude, high derivative noise in the raw tachometer signal. Even two small magnitude consecutive samples of differing sign and positive derivative will generate an erroneous zero crossing indication. The signal is therefore filtered with a low-pass FIR Remez filter. This is a constant group delay filter, so shifting the filter output by the group delay ensures zero crossing time remains uncorrupted. The noise is in the upper frequency reaches of the band, so filtering does not adversely affect any other aspect of the data. Close examination of Figure 4-6-top shows three small humps between the tachometer pulses. These are likely caused by electromagnetic coupling with the tachometer as the blades pass over the magnets. Since the derivative of these humps falls below the minimum derivative the zero crossing algorithm searches for, they need not be filtered.

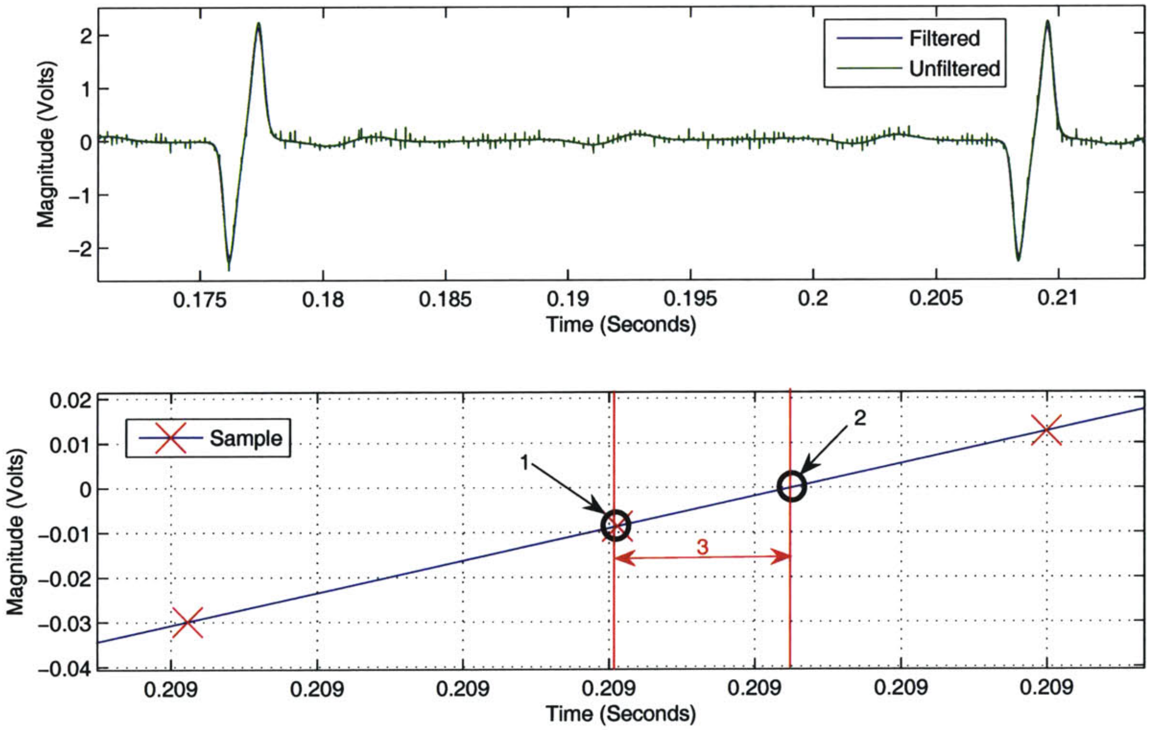

Figure 4-6: Filtered and unfiltered tachometer signal (top) and zoom of zero crossing point showing **1**–Sample before zero crossing, **2**–Interpolated zero crossing point, **3**–Distance from sample to zero crossing point.

DAQ Phase Shift Correction

All data channels are next windowed between two consecutive tachometer zero crossing points, as shown in Figure 4-7-top. The windowed data are then phase shifted according to DAQ channel by a fraction of a sample to correct for DAQ scan induced phase shift. The fractional sample shift is achieved by upsampling and sinc interpolating by the number of DAQ channels, shifting the desired channel by its channel number, then downsampling by the total number of channels. Figure 4-8 illustrates this phase shift by showing the result of sampling the same sine wave from four different DAQ channels.

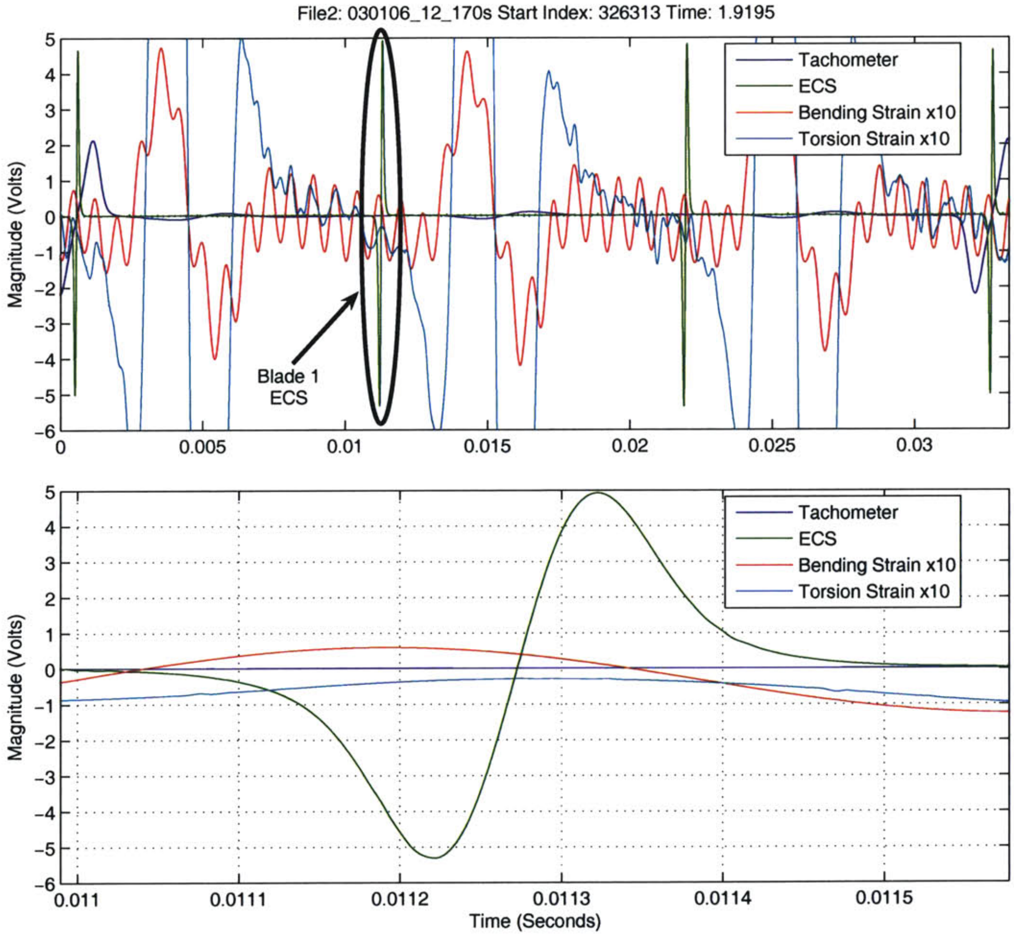

Figure 4-7: Example of one windowed revolution of data used to generate Figure 4-19 (top), zoom of blade #1 data window (bottom).

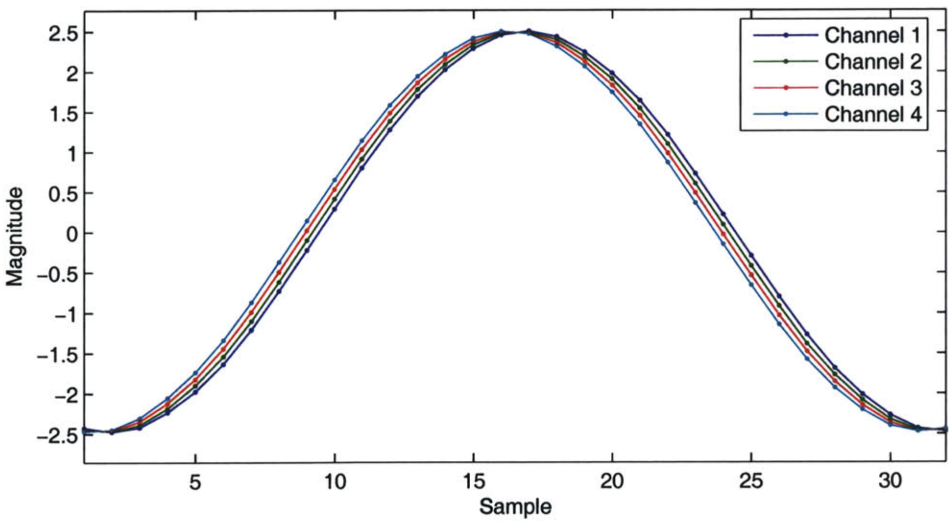

Figure 4-8: Example showing DAQ scan induced phase shift.

Second Stage Windowing

Once the data have been windowed between two tachometer pulses, the zero crossings of the ECS pulses must be found. Each ECS pulse corresponds to a blade on the rotor. The zero crossing of the pulse of the blade of interest is used as the center of a data window consisting of the ECS pulse and two channels of strain gage data (Figure 4-7-bottom).

Upsampling and Reprocessing

Although upsampling was performed for the DAQ phase shift correction above, the upsample factor was only equal to the number of channels in the data set. Since most data are taken with a tachometer, three strain gages, and three ECS sensors, at most seven channels are present, resulting in an upsample factor of seven. However, interpolation error decreases with higher upsample factors [16], so a factor larger than seven is desired.

To this end, all windowed data channels are further upsampled and sinc interpolated. Sinc interpolation allows for the perfect[2] reconstruction of arbitrarily many samples (Figure 4-9), subject to memory and processor limitations. Linear interpo-

---

[2] This does not take into account numerical and finite window error.

lation is still necessary, since many of the indices found using Equation 4.9 are not rational, and thus it is not possible to recover their exact value using sinc interpolation. However, the average error due to linear interpolation is reduced by a factor equal to the upsample ratio.

After upsampling and sinc interpolating, the zero crossings must be recomputed, since there will necessarily be additional samples between the previously computed zero crossing and the actual zero crossing. It is unlikely that any sample falls exactly on zero (Figure 4-9), so the ECS pulse is subsample shifted so that its zero crossing sample resides precisely on zero. This point will be used as a reference within the pulse for comparison with the second ECS pulse.

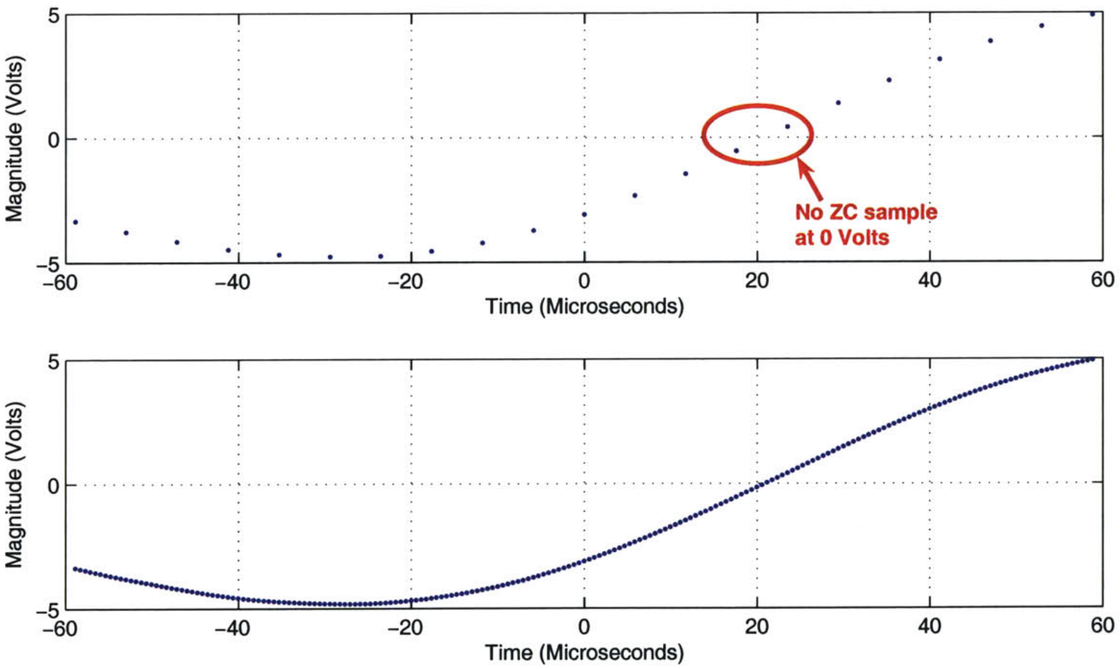

Figure 4-9: Window of ECS data sampled at 170KHz (top), window of ECS data upsampled to 1.70MHz (bottom).

Algorithm outline for processing comparison data:

10. Perform steps 1-9 to the baseline data.
11. Calculate time dilation ratio between baseline tachometer window and comparison data tachometer window.
12. Time dilate ECS data.
13. Subsample shift ECS data so zero-crossing point falls on integer sample.
14. Rewindow data around zero-crossing point.
15. Compute residue by subtracting processed baseline ECS pulse from processed comparison ECS pulse.

Time Dilation

Vibration detection must be accomplished independent of rotor speed. In particular, we would like to be able to compare baseline data at one speed with experimental data at a slightly different speed. Attempting a comparison between data collected at different shaft speeds without any transformation will yield results that are dominated by shaft speed related artifacts instead of features indicating a vibrating condition.

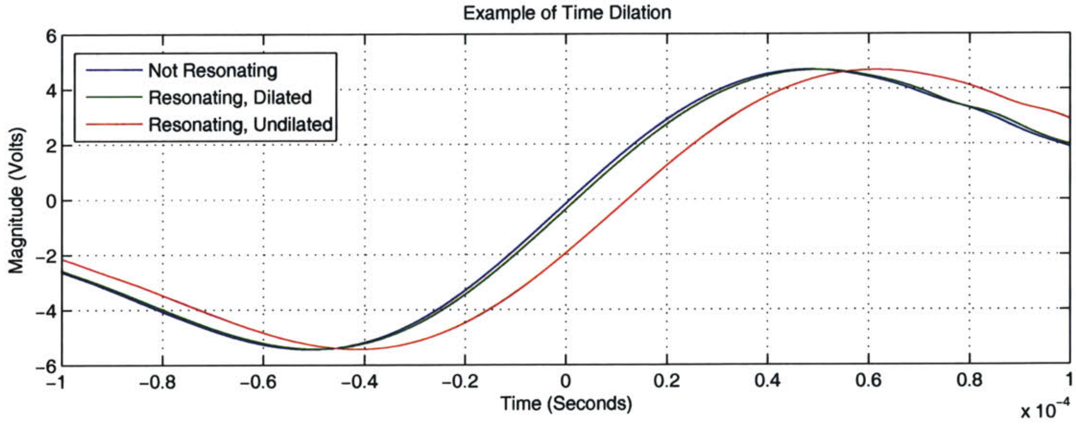

Figure 4-10: Example of baseline ECS pulse compared with dilated and undilated test pulse.

To account for such speed differences, a time dilation method is required. Time dilation works by resampling the data at a sample interval which is adjusted by the ratio of the number of samples, or time, in a single rotation of interest of each data set (Figure 4-10). Since the large number of samples per revolution makes lossless sinc interpolation impractical, some amount of imperfect interpolation is necessary during this procedure. In this case, the following standard linear interpolation was chosen:

$$d_{dil}(n) = d\lfloor\xi(n)\rfloor + (d\lceil\xi(n)\rceil - d\lfloor\xi(n)\rfloor) * (\xi(n) - \lfloor\xi(n)\rfloor) \tag{4.8}$$

where d is the data vector, and $\xi(n)$ is the irrational time dilation point to interpolate around.[3] Since time dilation is a cumulative operation, $\zeta(n)$ is used to find $\xi(n)$ as follows:

$$\xi(n) = \sum_{m=1}^{n} \zeta(m) \tag{4.9}$$

and $\zeta(n)$ is the time dilation vector defined as:

$$\zeta(n) = \frac{v(n)}{v_r(n)} \tag{4.10}$$

where $v(n)$ is blade velocity in the rotor frame, and $v_r(n)$ is shaft velocity.

To minimize interpolation error as much as possible, the signal to be dilated is first upsampled and sinc interpolated by a factor as large as memory and processor resources will allow. Since sinc interpolation can be used to generate an arbitrary number of perfect points, linear interpolation error is reduced by a factor equal to the upsample ratio.

4.3.2 Residue Characterization For Canonical Examples

Residue characterization plots were generated for four separate, representative cases. This was done to provide insight into residue behavior resulting from individual

---

[3] $\lfloor arg\rfloor$ denotes the floor of *arg* and $\lceil arg\rceil$ denotes the ceiling of *arg*.

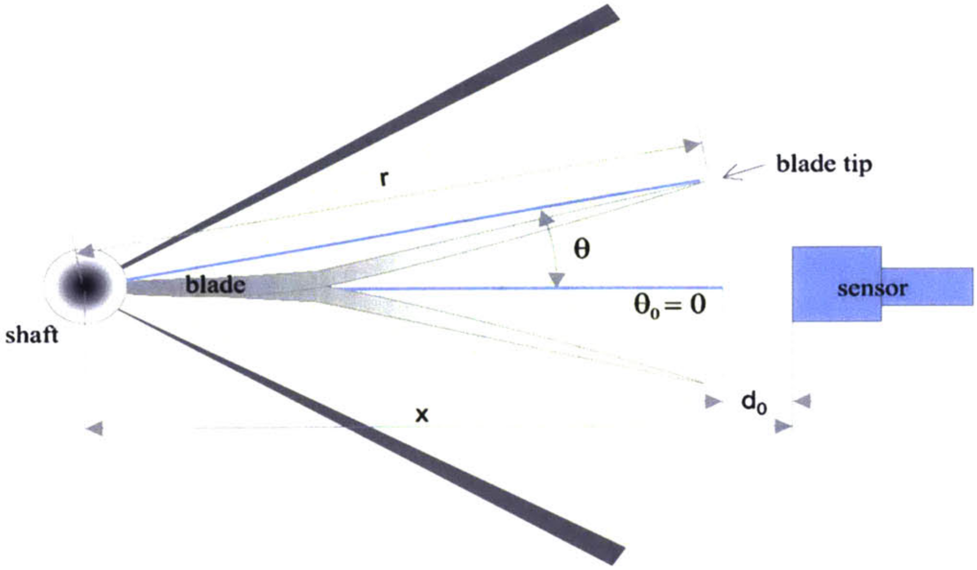

Figure 4-11: Diagram of shaft, blade, and sensor relationship [1].

changes in tip clearance, arrival time, velocity, and acceleration. The baseline model was based on the model developed by Teolis et. al. [1]. It assumes the ECS signal exhibits exponential decay with a zero crossing when the blade reaches the center of the sensor. For convenience, the model is expressed in the form of two equations.[4] The first represents sensor to blade tip distance:

$$d^2(\theta) = r^2 + x^2 - 2rxcos(\theta) \tag{4.11}$$

where d is blade tip to ECS sensor distance, r is shaft to blade distance, x is shaft to ECS sensor distance, and θ is blade tip angle. The second equation models the sensor itself:

$$g(\theta) = M_d \theta e^{-\beta d^2(\theta)} \tag{4.12}$$

where g is the sensor output function, M_d is an amplitude scaling factor, and β is decay rate. d^2 is the tip distance function in Equation 4.11. The output of these equations is shown in Figure 4-12. Although the model approximates the shape of an ECS signal well, there are discrepancies. One of the most important is that all of

---

[4] See Teolis [1].

the model's leading and trailing samples (roughly samples 1-250 and 750-1000) are zero. In a real ECS pulse, there are small but important non-zero undulations in these ranges (see Section 4.4).

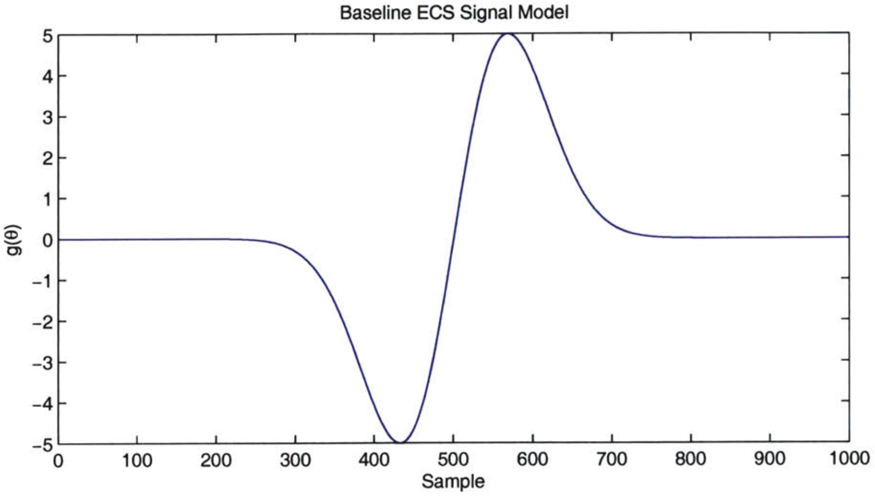

Figure 4-12: Canonical (baseline) ECS signal used for modeling.

Model Methods

Residue predictions were generated by modifying the canonical model of the baseline ECS signal to reflect how the signal is expected change under different conditions. The four basic conditions are blade tip clearance, arrival time, velocity, and acceleration. They are each modeled as follows:

i **Tip Clearance:** As the blade passes closer to the sensor (i.e. smaller gap), a higher magnitude signal is expected. Conversely, when the blade passes further from the sensor (i.e. larger gap) , a lower magnitude signal is expected. This is modeled by multiplying the baseline signal by an amplitude scaling factor, A. Values of A for a desired gap size can be calculated based on empirical ECS gap calibration data (see Appendix C). $A > 1$ indicates a smaller gap, and $A < 1$ indicates a larger gap.

$$s_{gap}(n) = A s_{base}(n) \tag{4.13}$$

ii **Arrival Time:** When the blade reaches the sensor early, the signal is expected to be a left-shifted version of the baseline signal. When it arrives at the sensor late, a right-shifted version of the baseline signal results. This is modeled by introducing a shift factor d into the original signal. Early arrival is modeled with $d < 0$ and late arrival is modeled with $d > 0$.

$$s_{arrival}(n) = s_{base}(n - d) \tag{4.14}$$

iii **Velocity:** Velocity is modeled by time compression or expansion of the base signal. Higher velocity corresponds to compression and lower velocity corresponds to expansion. This is modeled by introducing a constant time scaling factor, ζ, into the base signal. Higher velocity is modeled with $\zeta > 1$ and lower velocity with $\zeta < 1$. Since ζ is unlikely to be a rational number, interpolation is generally required (see equation 4.8).

$$s_{vel}(n) = s_{base}(n\zeta) \tag{4.15}$$

iv **Acceleration:** Acceleration is modeled similarly to velocity, except that ζ becomes a variable time dilation function $\zeta(n)$ instead of a constant. Constant acceleration corresponds to a linear change of velocity. A positive constant acceleration is therefore modeled with a linearly increasing $\zeta(n)$ function. To maintain constant mean velocity, $\zeta(n)$ is chosen so as to be odd symmetric with the constraint that $\zeta(n/2) = 1$. Negative constant acceleration (i.e. deceleration) is modeled in a similar manner, except that $\zeta(n)$ is chosen to be a linearly decreasing function. Since $\zeta(n)$ is now time varying, it is necessary to use the cumulative sum $\xi(n)$ defined in equation 4.9 to find each dilation point. $\xi(n)$ is also unlikely to be a rational function, so interpolation is generally necessary.

$$s_{accel}(n) = s_{base}(\xi(n)) \tag{4.16}$$

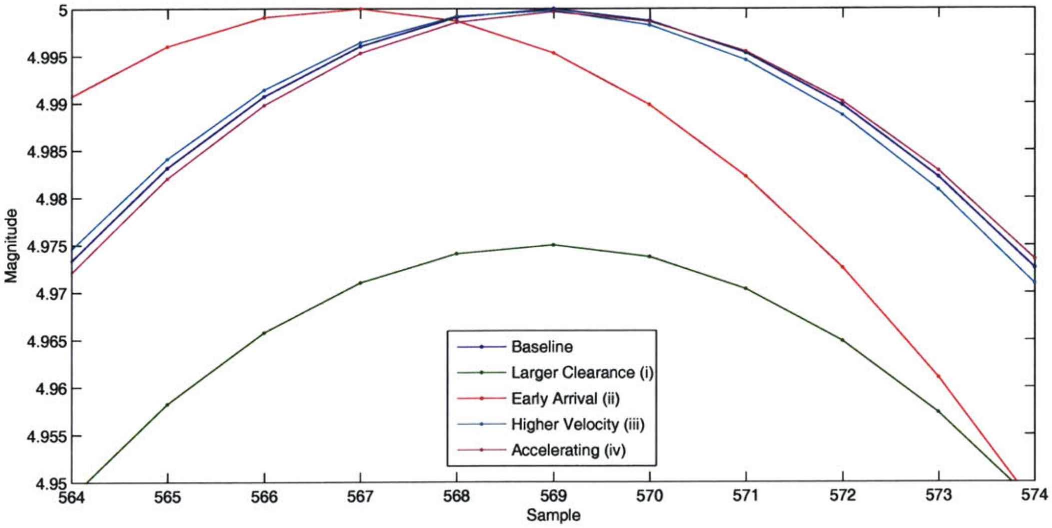

Figure 4-13: Comparison of 10 samples of simulated ECS signals.

Figure 4-13 shows a portion of the ECS signals that result from applying the above methods to the baseline ECS signal. The residual results of the model are shown in Figure 4-14. These plots depict residues derived by subtracting the modified signal from the base signal. This operation is represented mathematically as

$$r(n) = s_{base}(n) - s_{<mod>}(n) \tag{4.17}$$

where $r(n)$ is the residue, s_{base} is the canonical signal, and $s_{<mod>}(n)$ is the signal resulting from any one of operations i-iv.

Strain Based Simulation

Figure 4-14 shows the expected effects of a single component at a time (gap, arrival time, velocity, or acceleration). However, real data exhibit a combination of these components simultaneously. It is therefore necessary to develop a model capable of processing multiple components.

Since the strain gage data are proportional to displacement, they fully encapsulate the four components. Strain gage data are simulated using a sine wave:

$$g(n) = A_d \sin(2\pi W n + \psi) \tag{4.18}$$

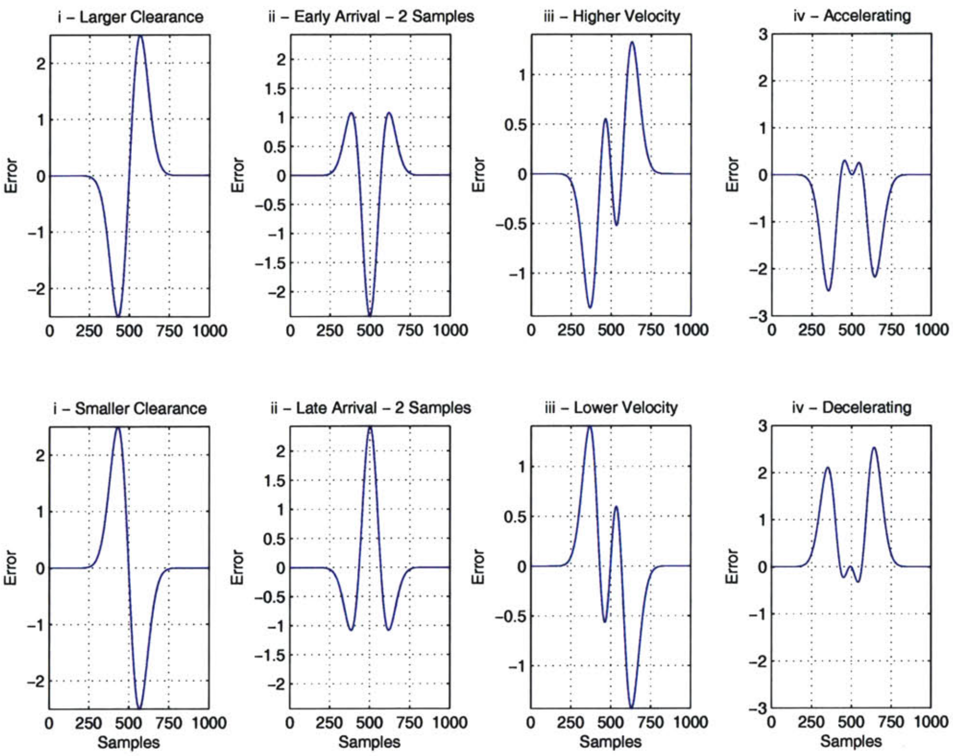

Figure 4-14: Simulation of residue based on canonical ECS model.

where $g(n)$ is the simulated strain signal, A_d is maximum strain or displacement, W is the frequency, and ψ is phase.

Velocity is found by taking the first difference and multiplying by sample rate, $v(n) = f_s(g(n) - g(n-1))$. Dividing by rotor velocity, a variable time dilation coefficient can be found as shown in Equation 4.10. Unlike the time dilation found in operation iv, this time dilation is non-linear, and encapsulates cases ii, iii, and iv. Nevertheless, the time dilation function $\zeta(n)$ can be processed in the same way as for case iv. Case i is carried through the simulation as a scaling factor since it does not involve any time dilation operations.

Figures 4-15 and 4-16 show an exaggerated sets of simulator inputs and outputs. The ECS signal and residue can be predicted for arbitrary strain signals. The effects of noise on the residue can also be simulated by introducing noise into the simulated strain gage data, the canonical ECS signal, or the simulated ECS signal. It is also possible to inject real strain data and a real baseline ECS signal into the simulator. The simulator can then be used to predict the observed ECS signal and residue (see

Section 4.4).

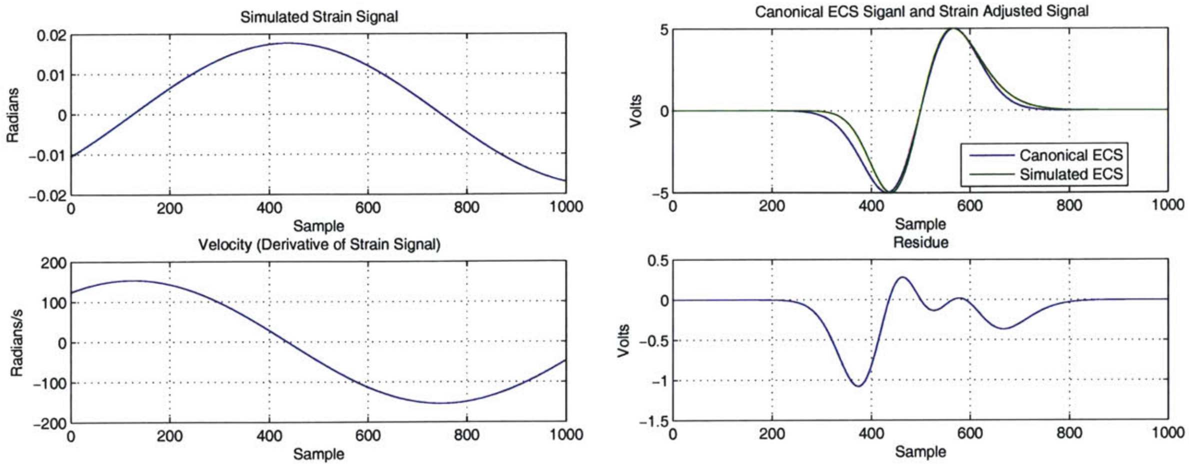

Figure 4-15: Strain based simulator input (left) and output (right).

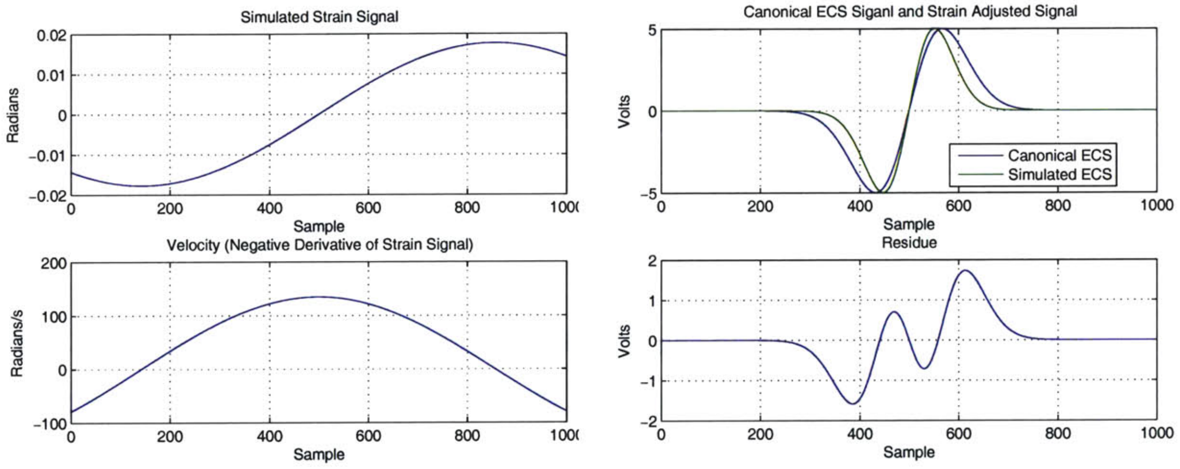

Figure 4-16: Strain based simulator input (left) and output (right).

4.4 Residue Characterization Method Results

What follows is a summary of the results of the residue characterization method. Each run of the algorithm is presented as a pair of plots. The top plot shows two normalized residues. The "Actual" residue is the residue generated by the algorithm from a pair ECS pulses taken from the empirical data. The "Predicted" residue is generated by running the strain based simulator with a baseline ECS pulse and the strain gage data as input. The simulator generates the residue prediction by transforming the baseline ECS pulse according to the strain gage data, and then subtracting the transformed pulse from the baseline pulse.

The bottom plot of each plot pair shows the strain gage data for the bending and torsion modes of each data set. These plots reflect actual measured displacement of the blades. The "File2" curves, which correspond to the excited data, are the data that are input into the strain based simulator to generate the residue prediction.

There are three primary parameters that distinguish the plots from each other:

- **Excitation Mode:** Determines the shape of the vibration. This can be either a bending mode or a torsion mode (see Section 3.1.1)

- **ECS Sensor:** Sensors #2 and #3 are separated rotationally in the spin pit by 90 degrees. Each sensor should therefore see the blade vibration at a different phase.[5].

- **Time Index:** Rotor speed is changing throughout the course of each run (Figure 4-17). By selecting different time indices from which to process ECS pulses from within a run, the algorithms can be tested at different shaft speeds from within the same data set. Stated another way, each of the plots represents data from a different revolution.

---

[5] It is possible, though unlikely, for both sensors to see the blade vibration at the same phase

4.4.1 Data Sets

Two data sets were used as input into the algorithm. Data set #12 was taken with the excitation magnets installed, and serves as the "comparison" data. Data set #15 was taken without the magnets installed, and is the "baseline" data set. Both data sets were taken using a step ramp speed profile (Figure 4-17). Within data set #12, both the second bending mode and first torsion mode were excited at different times (Figure 4-18). The unexcited data set was used to generate the baseline ECS pulses, and the excited data set was used for comparison.

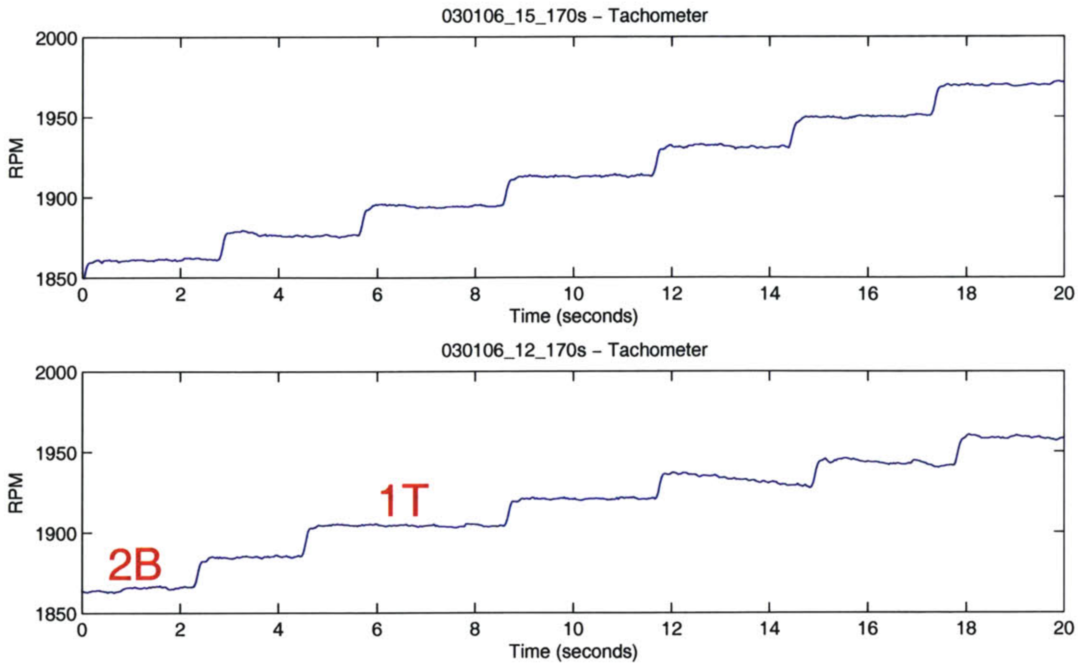

Figure 4-17: Unexcited ramp profile (top) and excited ramp profile (bottom) with vibrational modes noted.

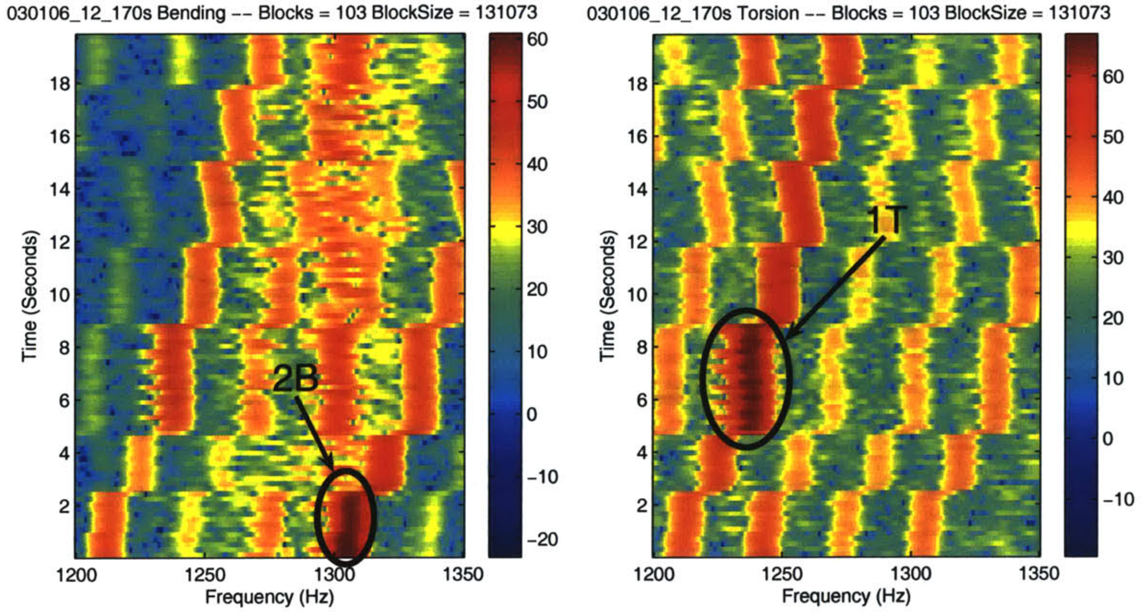

Figure 4-18: Vibrating data spectrograms showing bending mode excitation (left) and torsion mode excitation (right). "Step" shaped artifacts are caused by synchronous vibrations consistent with ramp profile.

4.4.2 Bending Mode Results

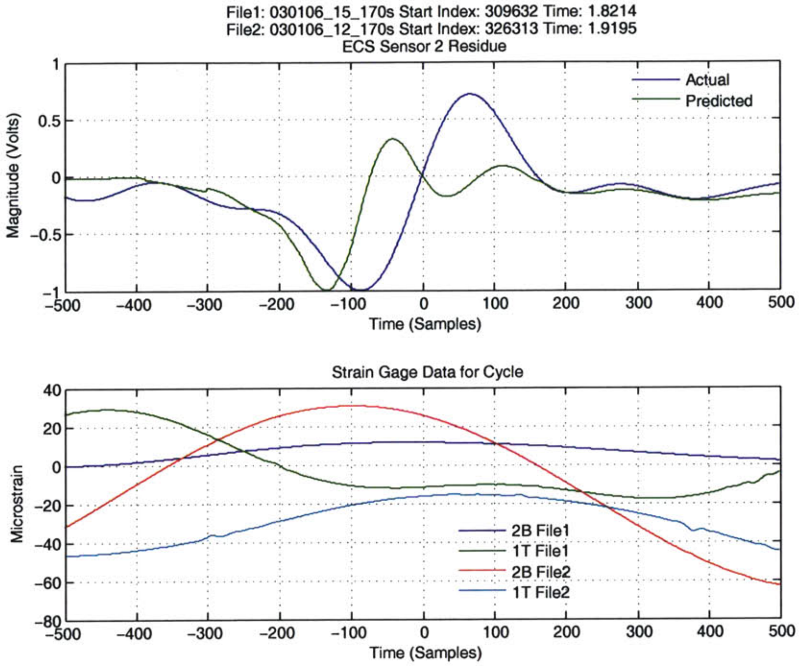

Figure 4-19: Bending residue characterization (ECS #2).

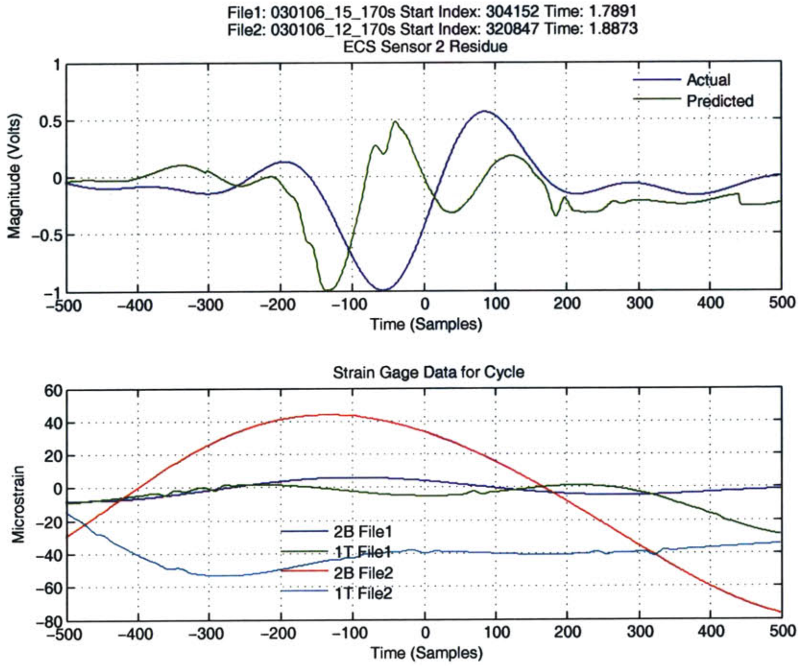

Figure 4-20: Bending residue characterization (ECS #2).

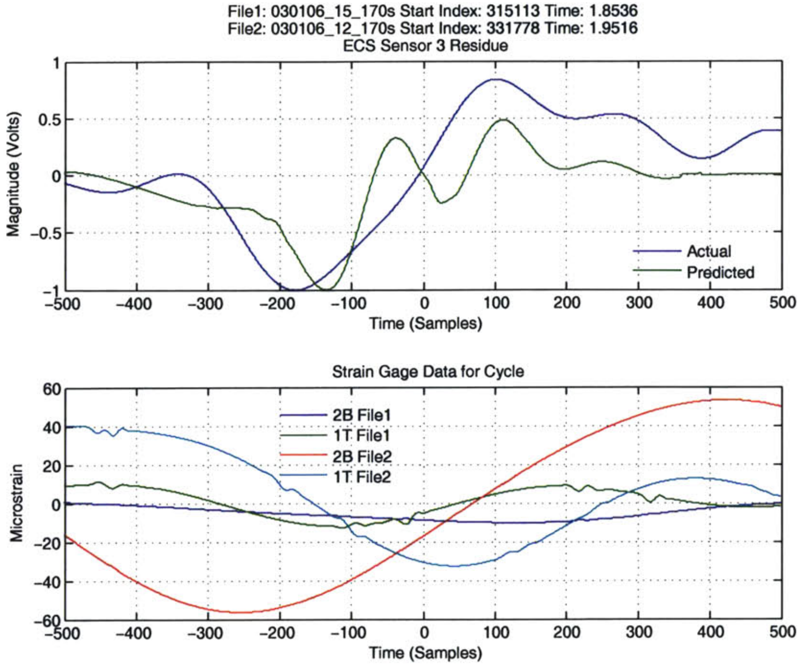

Figure 4-21: Bending residue characterization (ECS #3).

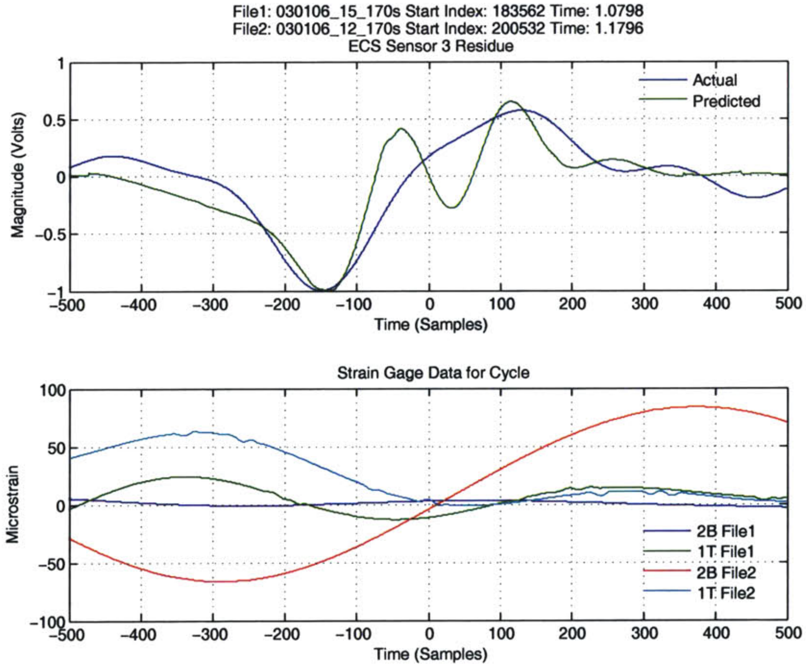

Figure 4-22: Bending residue characterization (ECS #3).

4.4.3 Torsion Mode Results

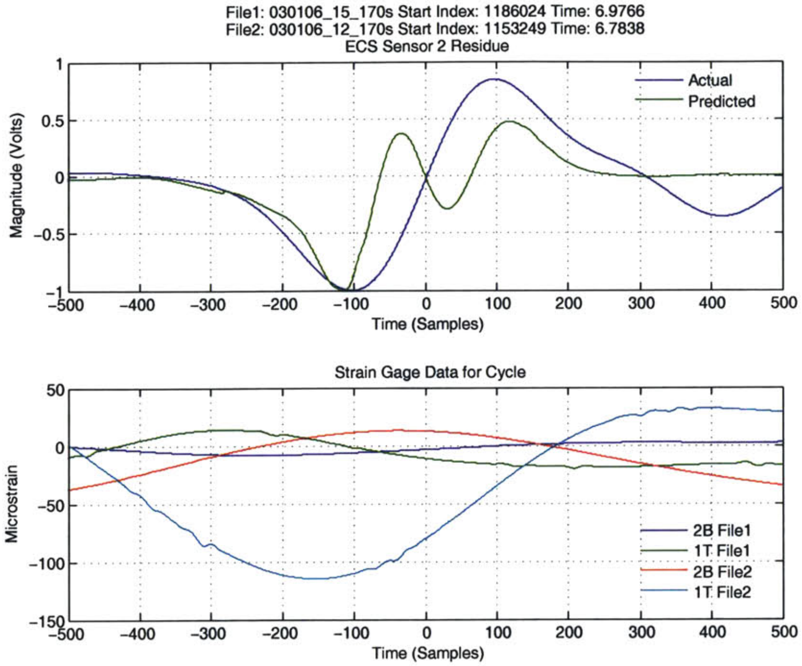

Figure 4-23: Torsion residue characterization (ECS #2).

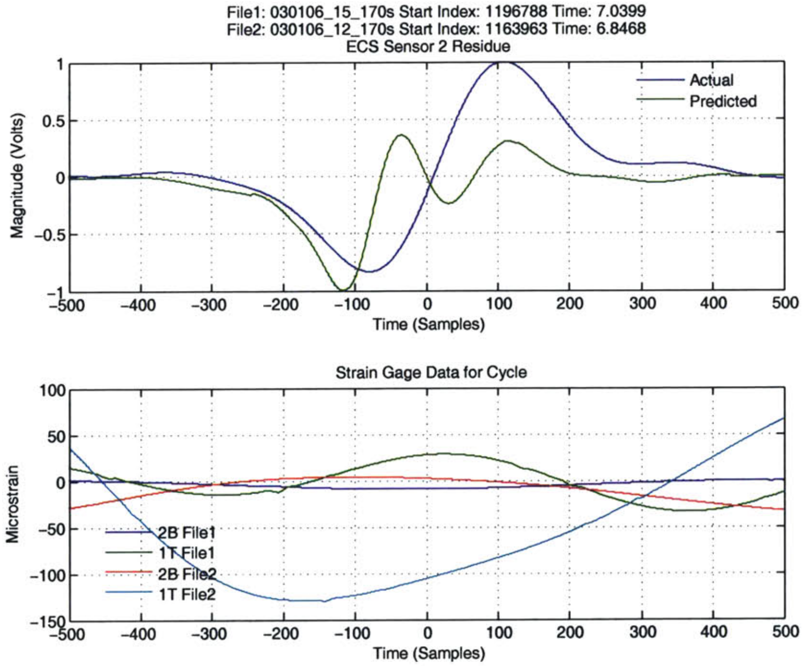

Figure 4-24: Torsion residue characterization (ECS #2).

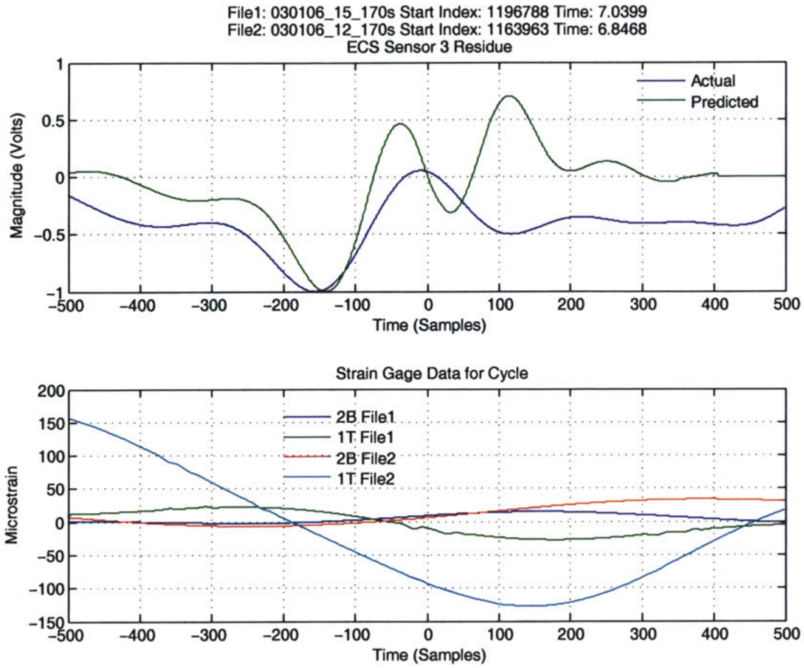

Figure 4-25: Torsion residue characterization (ECS #3).

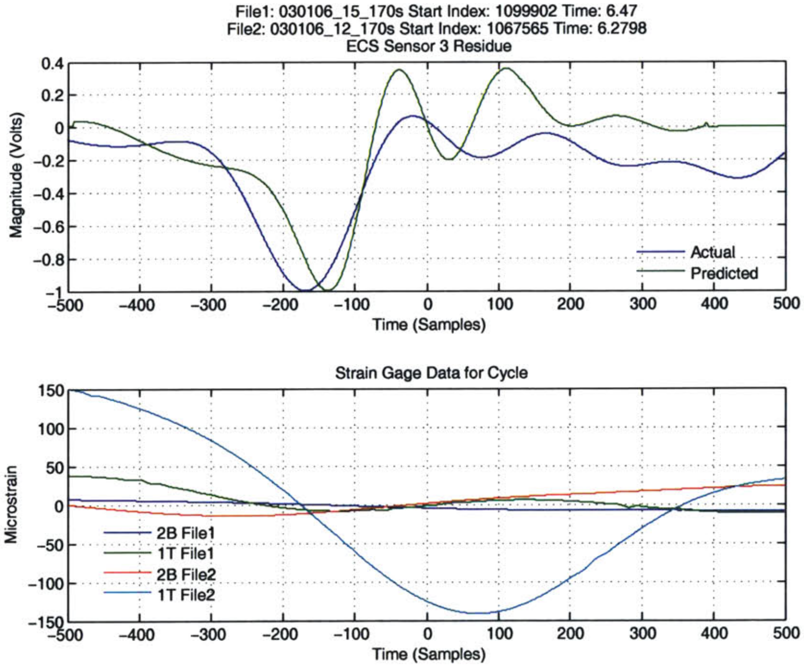

Figure 4-26: Torsion residue characterization (ECS #3).

4.4.4 Results Interpretation

The results for each mode will be analyzed. Before examining the residues, however, it is important to understand exactly how the blade is actually behaving. Each mode will thus begin with a discussion of the strain gage plots, which reflect directly measured blade behavior. The residues themselves will be addressed subsequently.

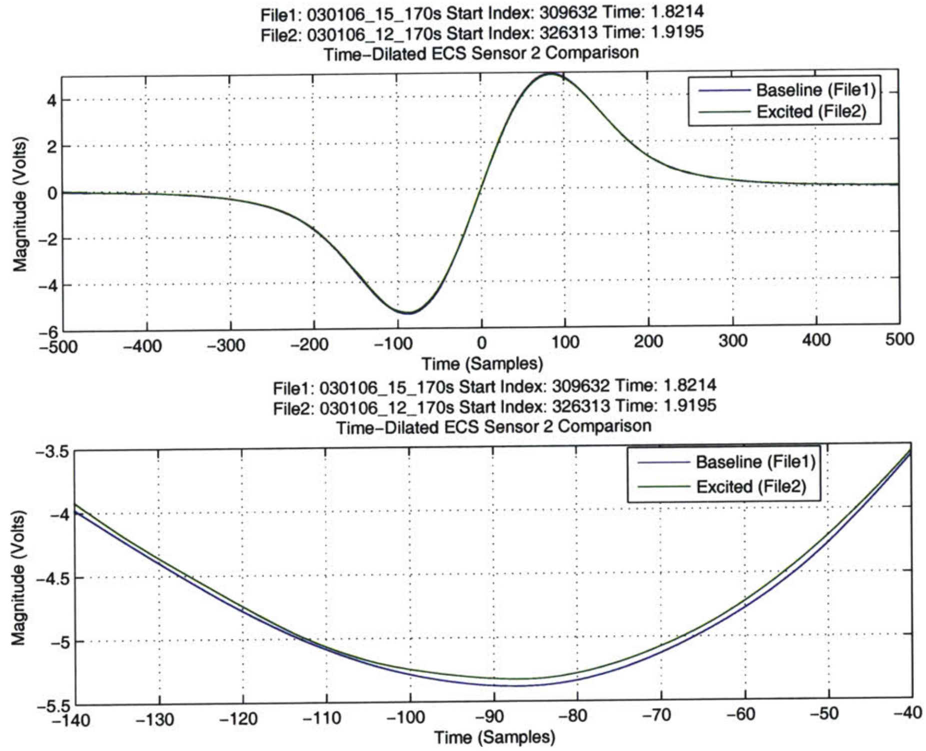

Figure 4-27: Processed ECS signals for Figure 4-19 (top) and 10x zoom (bottom).

Figure 4-27 shows the two processed pulses that generated the actual residue in Figure 4-19. It is included here to illustrate how similar the processed ECS pulses are and to provide context for the following discussion.

Bending Mode Strain Data

Looking at the strain gage data associated with the ECS #2 sensor position (Figures 4-19 and 4-20), it is evident that the largest magnitude strain is on the bending gage from the excited data, which is expected since this corresponds to a bending mode excitation. Comparing the two cycles, we see that the excited bending mode strains are in the same phase and are of roughly the same magnitude, indicating consistency across rotor cycles.

Strain data from the ECS #3 position (Figures 4-21 and 4-22) exhibit these same properties. However, the excited bending mode is approximately 90 degrees out of phase. This too is expected, and actually desired for experimental variability, since ECS #2 and ECS #3 are in different rotational positions in the spin pit. Note that there appears to be some out of phase excitation registered on the excited torsion gage. This may be caused by mechanical coupling between bending and torsion mode strain gages, which arises from their geometry. It is assumed to have a negligible effect for the purposes of these experiments.

Bending Mode Residue

Comparing the actual and predicted residues for ECS #2 (Figures 4-19 and 4-20), similar features are observed in both. The pulse widths are similar, and they both exhibit the same subtle trailing features from samples 200 to 500. The predicted residue in Figure 4-19 shows many of the same features as the actual residue, with one notable exception. There is an extra inflection centered around the origin, approximately 100 samples wide. This extra inflection also appears to contribute to a decaying phase shift error extending to the left and right from the origin. In fact, the extra inflection appears in all predictions, from all ECS sensors, and for both vibration modes. This suggests it is due to an algorithmic error. The decaying nature of the phase error extending away from the origin implies that it may be an error in the variable time dilation. Another possibility being considered is that it arises from a linear bias that is observed in the strain gage data. In the interest of avoiding repetition, the extra inflection will be omitted for the remainder of the section.

The actual residues for ECS #3 (Figures 4-21 and 4-22) are also consistent with one another. They differ from those of ECS #2 in that their pulse widths are wider, and they lack the sharp trailing edge transition starting around sample 100. These residue differences between the two ECS sensor positions are attributed to the phase difference between them. The predicted residues are very similar to the actual residues, showing many of the same features. However, there appears to be a constant error in the predicted residue in Figure 4-21.

Torsion Mode Strain Data

In all of the torsion mode plots, the excited torsion strain is clearly the highest magnitude strain. This is consistent with the fact that the rotor speed corresponds to a torsion excitation mode. Compared to the bending mode excitation, the torsion mode exhibits a longer wavelength, consistent with its lower frequency (1,222Hz vs. 1,294Hz for bending). However, the torsion mode strains do not show the same level of sinusoidal uniformity observed in the bending strains, particularly at ECS #2 (Figures 4-23 and 4-24). It is not clear why this is the case, although it could be caused by instrumentation problems. Like the bending mode case, the strains seen at ECS #3 (Figures 4-25 and 4-26) are approximately 90 degrees out of phase from those at ECS #2 (Figures 4-23 and 4-24). Similar non-uniformities in strain are noted between Figure 4-25 and Figure 4-26.

Torsion Mode Residue

The torsion mode residues exhibit similar correlations to the actual data as the bending mode residues. The extra inflection point is present, and appears to introduce a phase error that decays in both directions from the origin. Barring the extra inflection point, the prediction shows many of the features of the residue. In Figure 4-23, all features are represented with the exception of the trailing inflection point starting at sample 300. Figure 4-24 also displays all of the major features of the residue, however there is significant scaling error to the right of the origin.

The view from ECS #3 is similar. The prediction in Figure 4-25 shows strong feature correlation to the left of the origin, including subtle ripples. To the right of the origin, significant phase error, in addition to an offset error, is apparent. However the major features are still visible in the prediction. The prediction in the last plot, Figure 4-26, exhibits a small constant phase error throughout. Both major and minor features are present, however there is an offset error to the right of the origin similar to that seen in Figure 4-25.

4.4.5 Comparison To Pure Simulation

Since the bending strain is very close to an ideal sine wave, simulation was carried out treating it as such using the canonical ECS signal (Figure 4-12) as the baseline. Figure 4-15 shows the simulation results using a simulated sinusoidal strain with the same phase and frequency of the strain see at ECS sensor #2. The residue exhibits many of the features seen in Figures 4-19 and 4-20, including the major inflection and trailing ripples. It also shows the erroneous inflection point centered around the origin. Note that the leading and trailing 200 samples are zero, which is inconsistent with the data driven prediction. This is attributed to the fact that the canonical ECS signal does not exhibit the same perturbations as far away from the origin as the experimental ECS signal.

Figure 4-16 shows a similar simulation with the sinusoidal strain shifted to match the phase of the strain observed at ECS #3. The simulation results do not converge as conclusively as for the results seen at the ECS #2 position. However, the two peak magnitude humps correlate in position and relative magnitude. The trailing effects of the idealized ECS model are particularly apparent in Figure 4-21, since the actual residue exhibits a significant trailing non-zero offset.

4.5 Adaptive Filter Methods

An adaptive filter is a special type of filter that selects weights dynamically to minimize an error function. This allows the filter to adapt on the fly to different types of input signals. Figure 4-29 shows the adaptive filter is capable of accurately modeling both excited and unexcited ECS data. This is ideal for processing the baseline ECS signals for input into the residue characterization algorithm. The filter essentially maintains a moving widow of historic ECS data. In the event of significant change in the ECS signal, the filter model will provide historic steady-state data for comparison; the model will automatically adapt to the new ECS pulse shape over time, ensuring the residue characterization algorithm has an up to date model at all times.

Adaptive filtering was employed to compare the differences between vibrating and non-vibrating data. The adaptive filter algorithm is based on the block diagram in Figure 4-28.

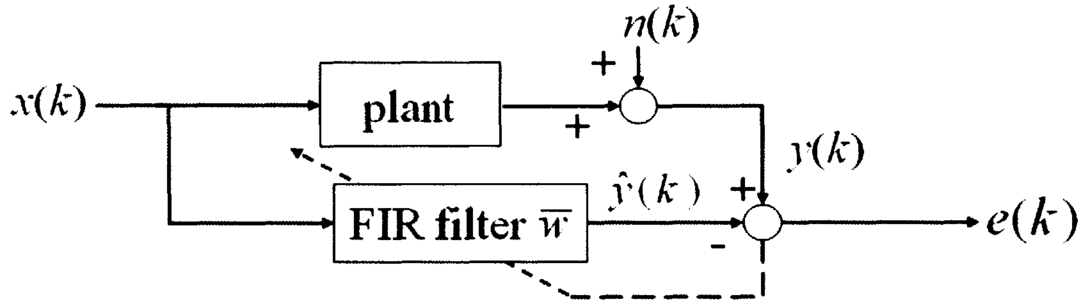

Figure 4-28: Block diagram of adaptive filter. $x(k)$ is an impulse train corresponding to zero-crossings of the tachometer, the plant is an ECS pulse, $n(k)$ represents noise, and $e(k)$ is the error.

The filter obeys the adaption law [21]:

$$\mathbf{w}_{k+1} = \mathbf{w}_k + 2\alpha e(k)\mathbf{x}_k \tag{4.19}$$

where $\mathbf{w}$ is a vector of filter weights, α is the adaption coefficient, and e is the error. $\mathbf{x}_k$ is defined as

$$\mathbf{x}_k = \begin{bmatrix} x(k) \\ x(k-1) \\ \vdots \\ x(k-p) \end{bmatrix}$$

where p is the filter order (i.e. the number of elements in $\mathbf{w}$). The error $e(k)$ is found by convolving the filter input with the filter coefficients and comparing the result with the plant [21]:

$$e(k) = y(k) - \hat{y}(k) = y(k) - \mathbf{w}^T\mathbf{x}_k \tag{4.20}$$

Equation 4.20 introduces $O(p^2)$ multiplications into the algorithm. However, since $x(k)$ is an impulse train, 4.20 can be simplified to

$$e(k) = y(k) - \tilde{\mathbf{w}}(k) \tag{4.21}$$

which eliminates the multiplications entirely.[6]

When the adaption is finished, the **w** vector approximates the ECS cycle signal within a boxcar window centered around the zero-crossing point. Figure 4-29 shows the result of the adaption for both vibrating and non-vibrating data. Figure 4-30 shows filter error as a function of ECS pulse cycle. The filter adapts extremely rapidly because the filter weight is initialized to the value of the first ECS pulse. Subsequent ECS pulses are similar, which explains the roughly constant error.

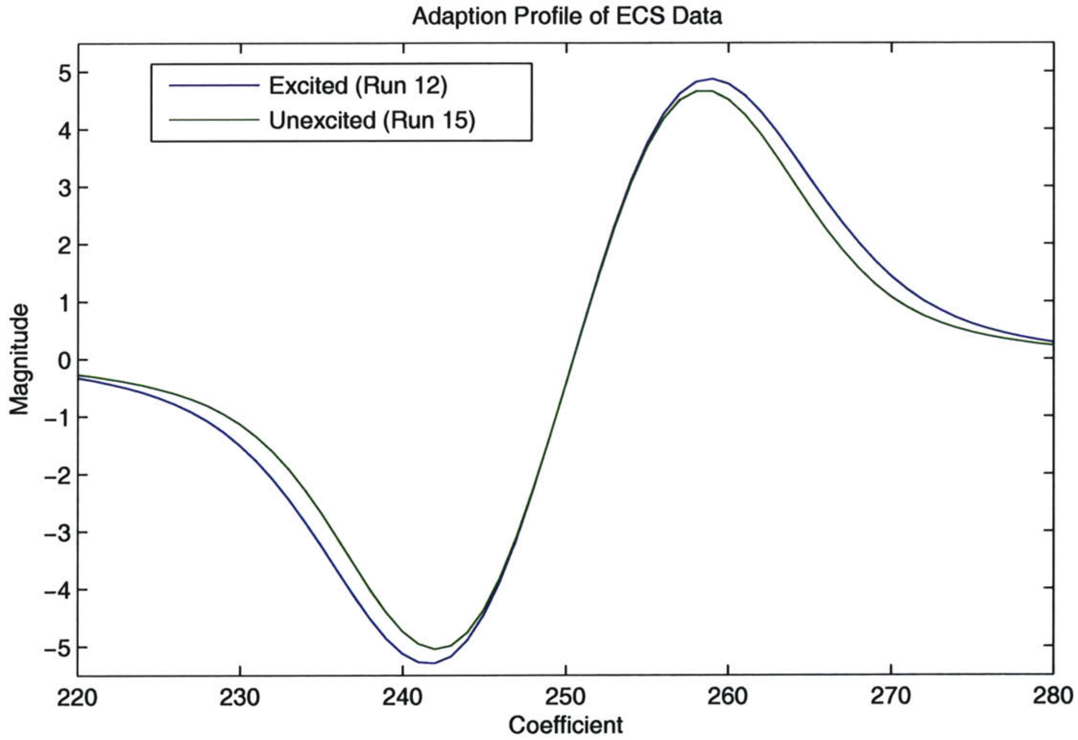

Figure 4-29: Comparison of vibrating vs. non-vibrating adaption.

---

[6] $\tilde{\mathbf{w}}(k) = \mathbf{w}(k \bmod p)$.

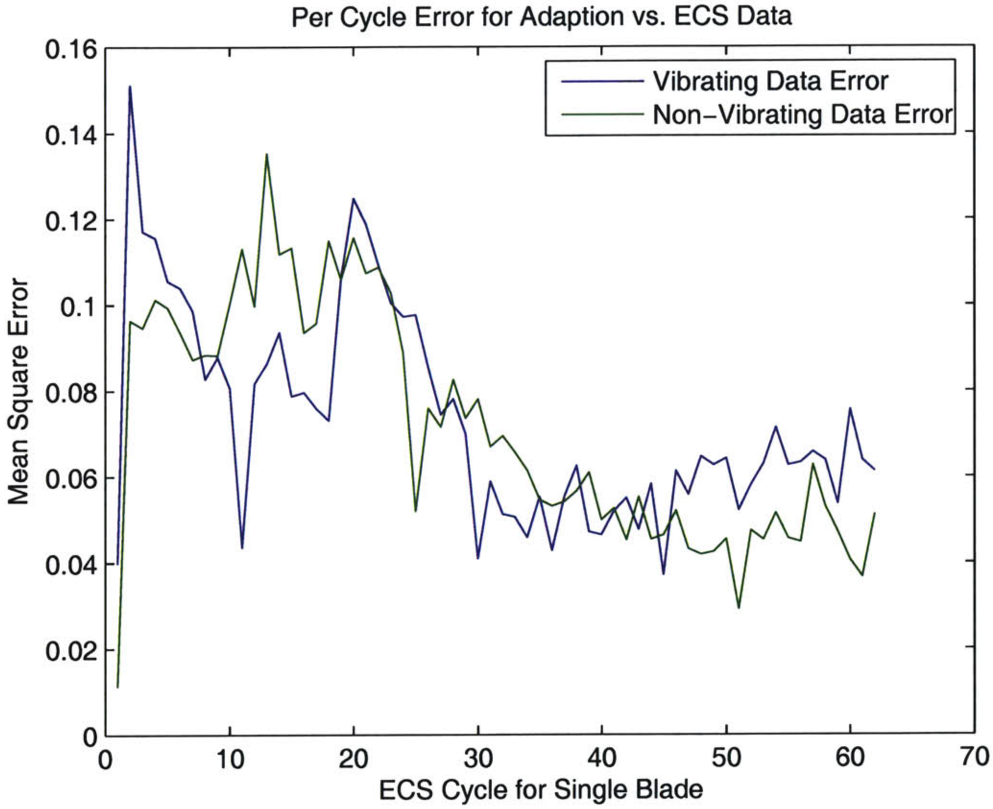

Figure 4-30: Per cycle adaption error.

Chapter 5

Conclusions and Future Work

5.1 Algorithms

The primary purpose of this research was the development and testing of algorithms suitable for vibration detection in turbomachinery. Existing techniques make use of only a small portion of the information available in an ECS signal, and often require multiple sensors. All of the methods developed in this research make use of all available data from a single sensor. The results are summarized in the following list.

- **STFT (Spectrogram) Analysis:** The spectrograms were an invaluable tool in reducing and characterizing the spin pit data. They were used extensively to examine wide speed sweeps and identify areas of resonance for subsequent narrow sweep runs. The spectrograms were also useful for identifying data sets with characteristics conducive to further analysis with the other algorithms. Further, spectrogram plots proved essential in characterizing and eliminating sources of sensor noise. This method is deemed to be ideal for first pass data analysis and characterization.

- **Hilbert Transform:** Hilbert transform techniques were applied in an attempt to derive blade vibration parameters from the ECS signal. It was hypothesized that such information may be contained in the instantaneous frequency representation derived from the Hilbert transform. Unfortunately, this method proved highly susceptible to noise, and does not lend itself to analyzing signals with numerous frequency components. It was thus concluded that this is not an effective method for processing the ECS signal.

- **Residue Characterization:** The residue characterization method is a novel technique developed in the course of this research. It is based on processing the ECS signals to allow direct comparison in the form of a residue. The algorithm was applied to a number of data sets, and was found to generate consistent results. A simulator was developed to relate measured blade behavior from the strain gages to these results. With the exception of an extra inflection point around the origin, the simulator consistently generated reasonable predictions reminiscent of the ECS residue using only strain gage data and a baseline ECS pulse. This implies that after some additional tuning of the method the inverse problem of deriving blade displacement from ECS pulses can be solved.

- **Adaptive Filtering:** An adaptive filter algorithm was implemented and applied to the data. Adaptions to both excited and unexcited data were successfully performed. While this cannot be used to determine blade vibration alone, it can be extremely powerful when combined with the residue characterization method, especially as a preprocessing step as in Figure 1-1.

5.1.1 Future Work

Although the Hilbert Transform methods did not produce good results in this research, there remain a number related techniques that may facilitate better results. First, the data can be preprocessed and filtered to eliminate the dominant pitch signal. Then, the various frequency components can be separated using Empirical Mode Decomposition [20]. These signals could then be analyzed with the Hilbert transform methods and the results evaluated.

The residue characterization method shows the most promise. The first goal of any future development should be investigation and elimination of the extra inflection point in the simulator output. Next, quantitative correlations should be computed between the actual and predicted residues. Then, an inverse transform simulator should be developed. This will enable the synthesis of displacement data from the two ECS signals alone. From this, it is possible to derive vibration parameters such as frequency and vibrational mode. Once this has been done, the adaptive filter algorithm can be integrated into the data stream. The adaptive model will serve as the baseline ECS signal for the residue characterization method. This provides a baseline model that changes over time, while averaging out uncorrelated noise.

5.2 Data Collection

- **Spin Pit:** A significant quantity of data was collected to support algorithm development and testing. Approximately 27 minutes of data were taken with the Mk3 blisk, and 136 minutes of data were collected from the three-bladed rotor. Each rotor had data taken with a combination of sensors, including tachometer, strain gages, and multiple ECS sensors. VRS data were taken during some of the Mk3 blisk runs.

  Each rotor was run over a wide range of speeds. Some data were collected over wide speed ranges using low sample rates, while other data were taken with narrower speed ranges but higher sample rates. Runs were also conducted using step ramps. This allowed a single run to generate multiple blocks of constant speed data. All of the data are organized on a website with a consistent file and directory naming scheme.

- **Spectrogram Plots:** Spectrogram plots visually depict the signals of the different sensors as a function of time and frequency. The automated spectrogram generation suite was used to generate a set of 15-20 spectrogram plots for each data set. This allows one to view the entire contents of a data set, from all sensors, at a glance. The spectrograms are arranged in directories whose name contains the name of the data file from which they were generated.

- **Hammer Test Results:** Both rotors underwent extensive hammer testing.

The data were collected using the spectrum analyzer, and thus only frequency domain data are available. These data are organized similarly to the spin pit data on the web server.

- **Algorithm Results:** Each algorithm was automated and run on many different data sets. This resulted in literally thousands of plots which comprise the results. These plots are organized according to algorithm, the data set they were generated from, and and the offset used to index into the data.
- **Matlab Scripts:** All Matlab scripts are posted on the website. These scripts include spectrogram generation routines, adaptive filtering, Hilbert transform algorithms, residue characterization methods and simulation, data manipulation, and various ancillary utility scripts.
- **Documentation:** Documentation describing the column arrangement of each data set is included with the data itself. Additional documentation includes Hood data formats, test plans, conference call minutes, presentations, and equipment specifications.
- **Photographs:** Large numbers of photographs were taken of all aspects of the data collection process. These include spin pit operation, bearing replacement, equipment setup, rotor instrumentation, and spin pit repair. These photographs are organized according to data and subject matter.

5.2.1 Future Work

Spin Pit

Although significant maintenance and repairs were performed on the spin pit and associated equipment during the course of this research, a number of pressing issues still exist.

- **Wiring Hub:** The wiring hub that interfaces the rotor to the slip ring must be rebuilt before any additional data collection. Metal from the rotor has cut into much of the internal hub wiring. This manifests itself in the data as significant electrical noise. The problem was temporally corrected using tape, however, this is clearly a short term solution.

- **Strain Gage Connectors:** The small electrical connectors on the lower part of the wiring hub do not lend themselves to high speed operation. Above 3,000 RPM, centrifugal force results in the female strain gage plugs tearing off the rotor, often taking additional wiring and strain gages along with them. Silicon RTV was used to secure the plugs for the purposes of this research, however, these connectors should be replaced with some form of locking connector. It should also be noted that the existing connectors are proprietary and no longer available.

- **DAQ:** The current DAQ setup is inadequate. The computer lacks the resources for sustained high sample rate operation. This led to repeated crashes and data loss throughout the course of this project. At a minimum, the computer must be replaced. If possible, a higher performance DAQ card should also be acquired.

Time Domain Hammer Test Data

The existing hammer test setup only records data on the spectrum analyzer. The raw hammer test data are therefore not recorded, only the results of the averaged FFT of the data. While this is useful for real-time determination of the mode frequencies, large amounts of data are lost in the FFT process, depending on the settings of the spectrum analyzer. Parameters such as resolution, window length and type, and triggering can all have an adverse effect on the quality of data taken. Moreover, there is no operational need to obtain the FFT results in real-time.

The data quality can be improved by collecting time-domain data using the DAQ. A LabView virtual instrument must be developed that triggers on the hammer load cell, and records data for a desired amount of time for each impulse. These data can then be transformed and averaged in post-processing. It would be useful for such a system to be able to record data from multiple strain gages simultaneously. This would allow different modes, such as torsion and bending, to be recorded simultaneously from a single hammer tap.

Appendix A

Test Plan

Table A.1: Example of an actual test plan

Test	*Quantity*	*Sweep RPM*	*Sample Rate*	*Sensors*
01	15	1500-2500	20KHz	Tach, Strain
02	05	2250-2450	100KHz	Tach, Strain, ECS
Remove blade and reinstall				
03	02	1500-2500	20KHz	Tach, Strain
04	01	2250-2450	100KHz	Tach, Strain, ECS
Remove blade and send to PW.				
Install returned blade.				
05	02	1500-2500	20KHz	Tach, Strain
06	01	2250-2450	100KHz	Tach, Strain, ECS
Remove blade and send to PW.				
Install returned blade.				
07	02	1500-2500	20KHz	Tach, Strain
08	01	2250-2450	100KHz	Tach, Strain, ECS
Change magnet air gap.				
09	02	1500-2500	20KHz	Tach, Strain
10	01	2250-2450	100KHz	Tach, Strain, ECS
Return air gap to original distance.				
Remove blade and return to PW.				
Install returned blade.				
11	02	1500-2500	20KHz	Tach, Strain
12	01	2250-2450	100KHz	Tach, Strain, ECS
Change magnet air gap.				
13	02	1500-2500	20KHz	Tach, Strain
14	01	2250-2450	100KHz	Tach, Strain, ECS
Return air gap to original distance.				

Appendix B

Pratt & Whitney Vibrometer Testing

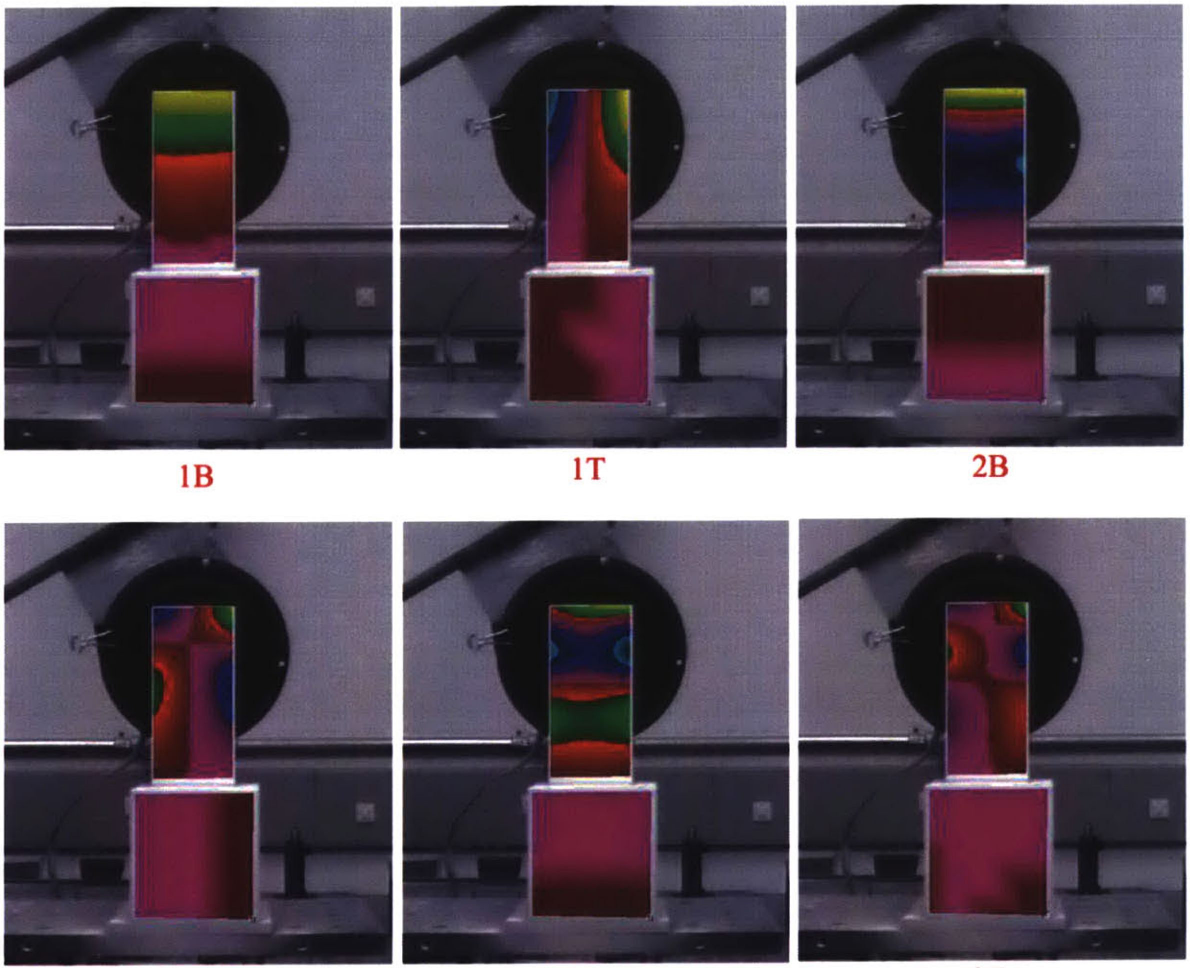

1B 1T 2B

2T 3B 3T

Figure B-1: Pratt & Whitney vibrometer test results.

Appendix C

ECS Sensor Clearance Calibration

Since ECS sensors respond differently, it is necessary to calibrate the sensor at various different gap sizes (d_0 in Figure 4-11). The process was to set the gap between the sensor and blade tip using a set of machinist's gages. For each gap setting, the spin pit was run at four different shaft speeds, 10, 20, 30, and 40 Hertz. Fourteen runs were required to capture the full dataset. Data were collected for each combination of speed and gap. The results are summarized in Table C.1.

From Figure C-1, it is observed that the ECS output signal tapers off exponentially with increasing gap size. The signal is not significantly affected by rotor speed. Equation C.1 shows the exponential function fitted to the data:

$$A(d_0) = 44.55e^{0.024d_0} \tag{C.1}$$

where A is the ECS pulse maximum amplitude and d_0 is the tip clearance in mils.

Table C.1: ECS sensor gap calibration results.

Gap (mils)	*Magnitude (Volts)*			
	10Hz	*20Hz*	*30Hz*	*40Hz*
70	8.04	8.06	8.18	8.27
80	6.91	6.85	6.99	7.16
90	4.79	4.82	4.86	5.00
100	3.79	3.73	3.79	3.85
110	2.93	2.93	2.94	2.98
120	2.37	2.41	2.44	2.49
130	1.92	1.94	1.97	2.01
140	1.52	1.55	1.56	1.60
150	1.26	1.26	1.29	1.32
170	0.87	0.86	0.87	0.87
190	0.61	0.61	0.61	0.62
210	0.49	0.49	0.50	0.50
230	0.36	0.35	0.34	0.35
250	0.28	0.28	0.26	0.27

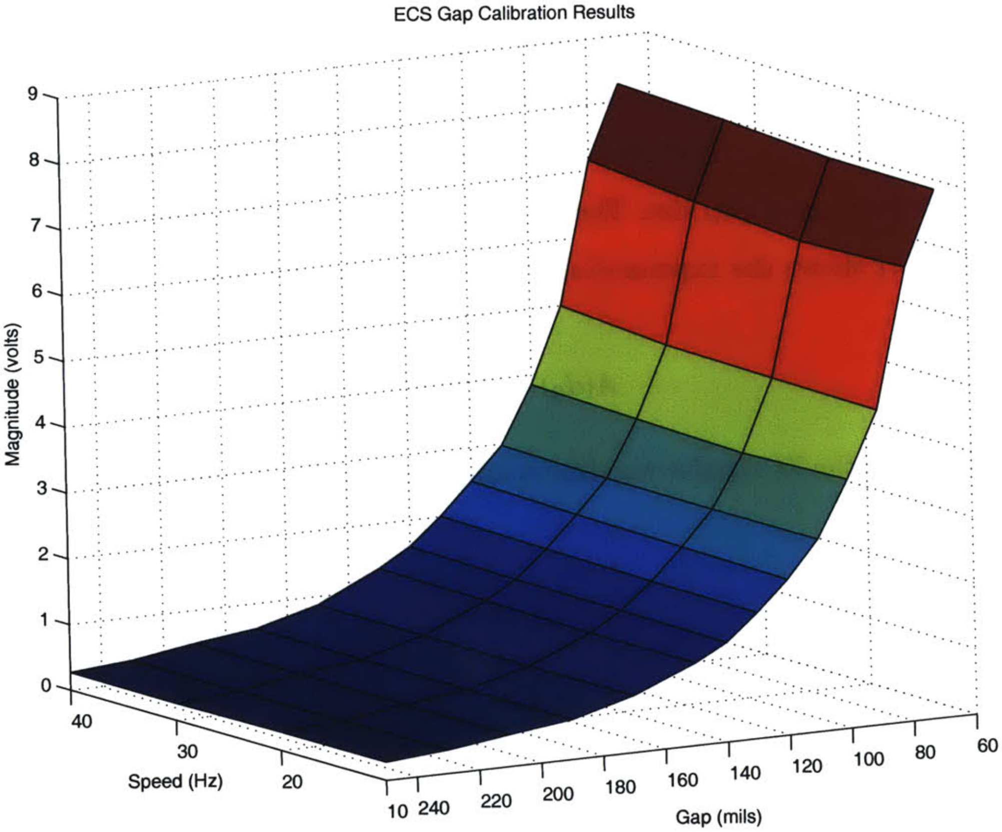

Figure C-1: Plot of ECS calibration data.

Appendix D

Hood Technologies Equipment

Two specialized instruments were provided by Hood Technologies to support data collection and analysis. These are an order tracking system and a tip-timing system.

D.1 Order Tracking

Hood provided a real-time order tracking system to facilitate data collection. The system consists of a laptop computer connected to a four channel DAQ. The DAQ inputs are the tachometer and the three strain gages (bending, torsion, and stiffwise bending). A Matlab script processes the incoming data in real time, and displays the response for the selected orders at each sensor (Figure D-1). This response plot represents magnitude as a function of an integral multiple of shaft speed. It can be used to localize the shaft speed to an area of large response.

While three selected orders are displayed in real time, all specified orders are saved in a Matlab binary file for later analysis. The file contains a large matrix called DATA that contains the RPM history along with the response for each order and each sensor. The response is stored in complex notation, so both angle and phase can be easily calculated.

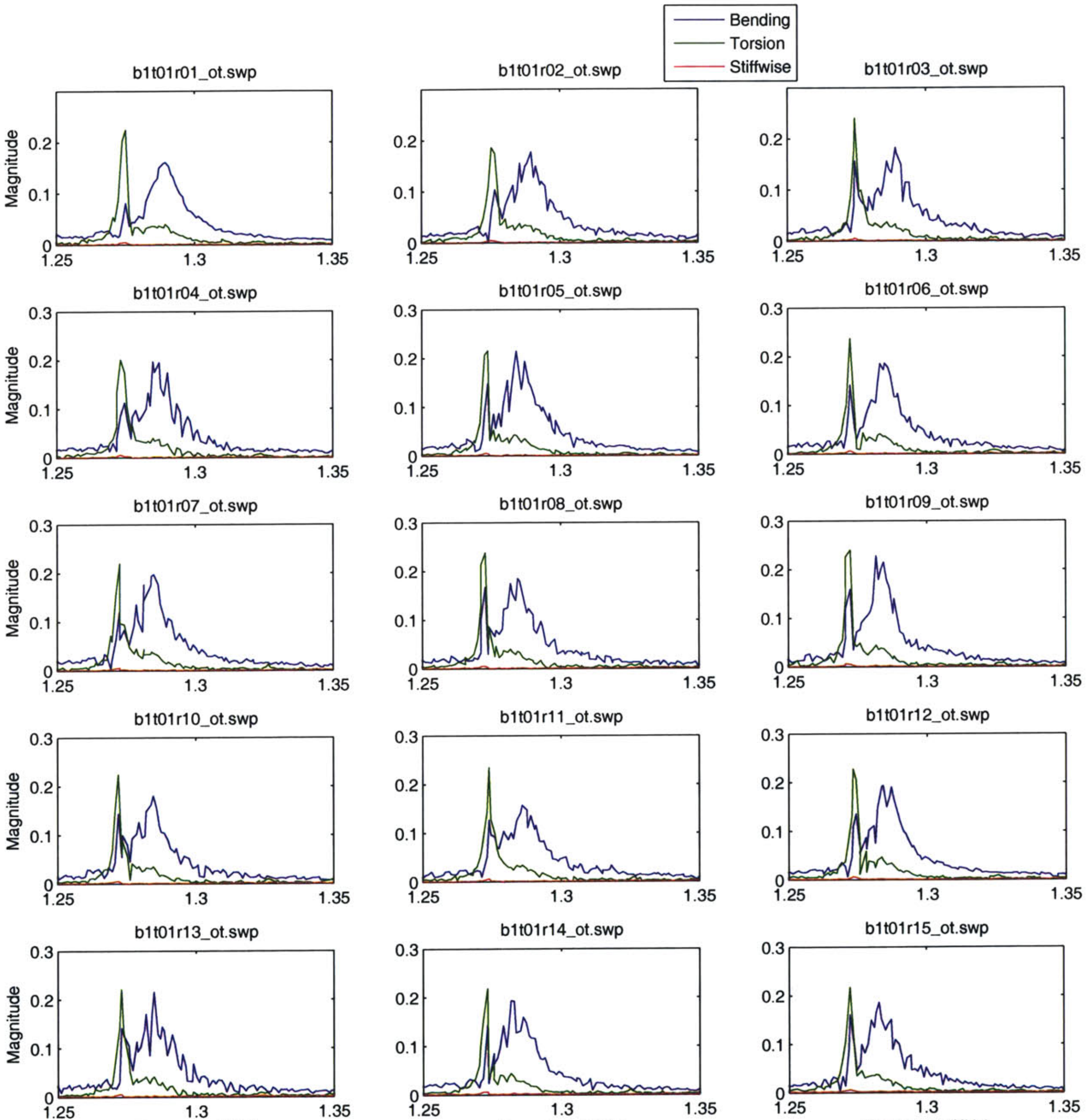

Figure D-1: Order 33 plots for series of runs of 3-bladed rotor.

D.1.1 Quality Factor

Order tracking data are also useful for finding the quality factor of the blade signal. In this case, quality factor is defined as the resonant frequency divided by the bandwidth at the half-power point:

$$Q = \frac{f_r}{f_2 - f_1} = \frac{f_r}{\Delta_f} \tag{D.1}$$

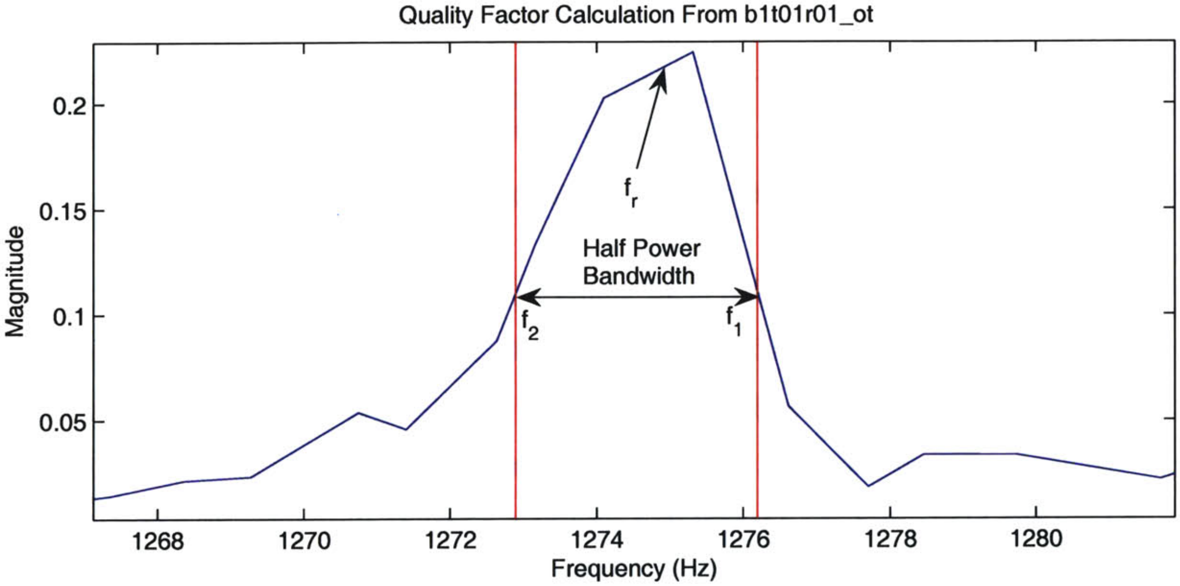

Figure D-2: Quality Factor calculation from data.

D.2 Tip Timing

Hood also supplied a very accurate tip timing system similar to that described in Section 1.1.1. This system uses a special analog circuit to detect the exact moment of zero-crossing of the ECS signal. Although zero-crossing times can be derived from the DAQ data, it is not as accurate. The DAQ samples at fixed intervals, so it is likely that the zero-crossing will occur between samples, necessitating an interpolation to derive the actual crossing time. The analog circuit in the Hood system is asynchronous, so it triggers precisely on the zero-crossing and generates a time stamp. While tip timing information can be derived from the data recorded by the

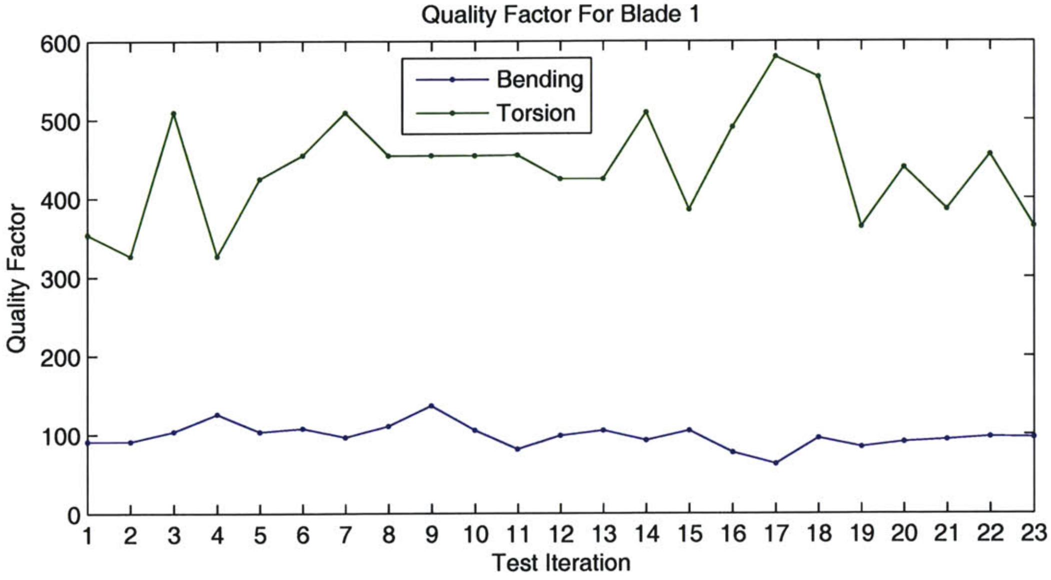

Figure D-3: Quality Factors for three-bladed rotor.

DAQ, significant interpolation error would be expected.

Data from the Hood timing system is stored in a series of proprietary files. These files can be loaded and the data manipulated using the Hood supplied Analyze Blade Vibration program (Figure D-4). This program can plot the zero crossing delta between the blade and the tachometer, and fit a curve to this data. The resulting plot shows blade displacement in thousandths of an inch as a function of rotor speed. A set of Matlab scripts was also developed with Hood to load the data into Matlab. These scripts allow for the extraction of the raw timing data from the proprietary Hood files.

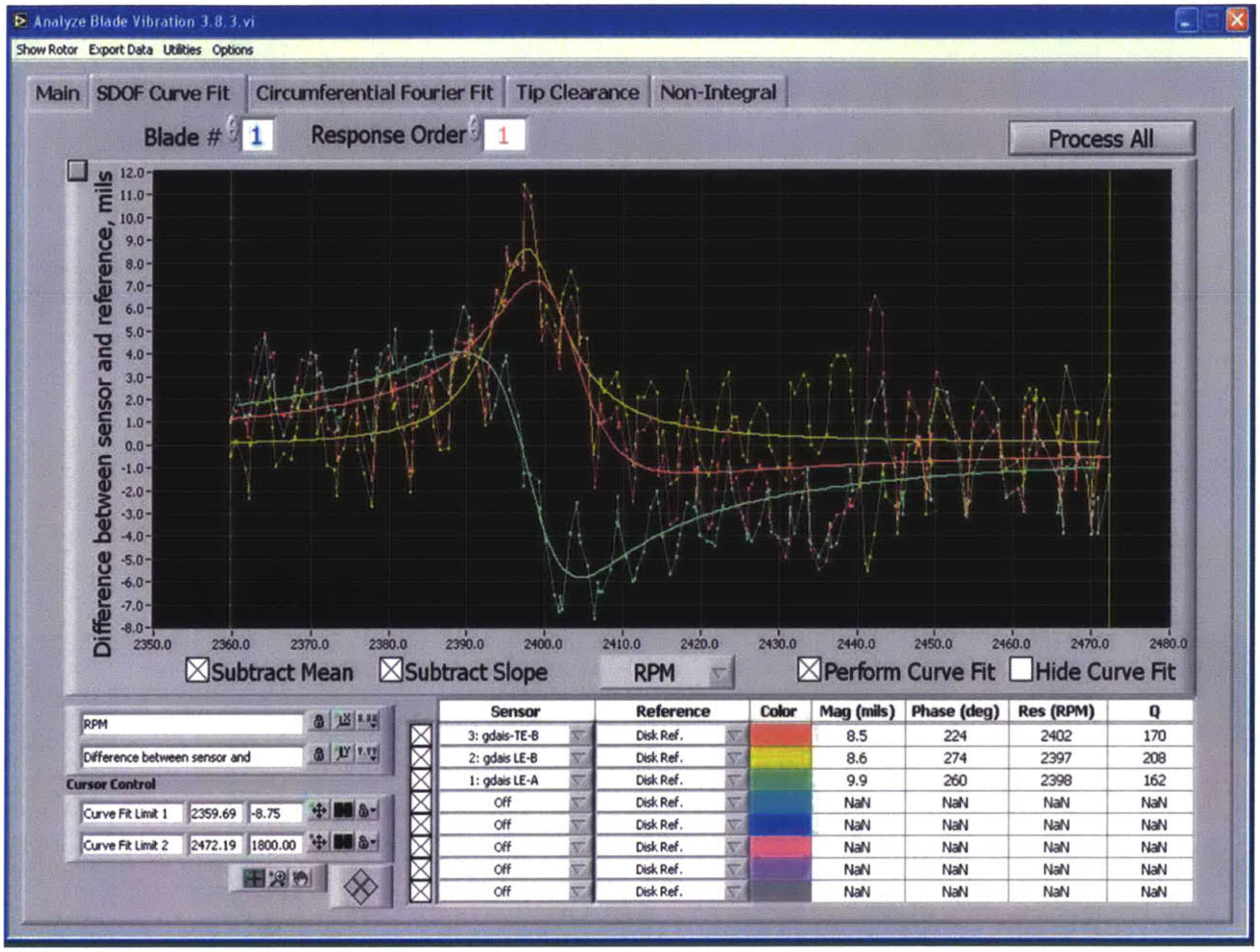

Blade # 1 Response Order 1

☒ Subtract Mean ☒ Subtract Slope RPM ☒ Perform Curve Fit ☐ Hide Curve Fit

RPM

Difference between sensor and

Curve Fit Limit 1	2359.69	-8.75
Curve Fit Limit 2	2472.19	1800.00

	Sensor	Reference	Color	Mag (mils)	Phase (deg)	Res (RPM)	Q
☒	3: gdais-TE-B	Disk Ref.	🟥	8.5	224	2402	170
☒	2: gdais LE-B	Disk Ref.	🟨	8.6	274	2397	208
☒	1: gdais LE-A	Disk Ref.	🟩	9.9	260	2398	162
☒	Off	Disk Ref.	🟦	NaN	NaN	NaN	NaN
☒	Off	Disk Ref.	🟦	NaN	NaN	NaN	NaN
☒	Off	Disk Ref.	🟥	NaN	NaN	NaN	NaN
☒	Off	Disk Ref.	🟪	NaN	NaN	NaN	NaN
☒	Off	Disk Ref.	⬛	NaN	NaN	NaN	NaN

Figure D-4: Hood tip timing analysis.

Bibliography

[1] C. Teolis, A. Teolis, J. Paduano, and M. Lackner. Analytic representation of eddy current sensor data for fault diagnostics. In *Aerospace, 2005 IEEE Conference*, pages 1–11, 2005.

[2] Invensys, Pawtucket, RI. *Introduction to variable reluctance sensors (VRS).*

[3] Matthew Lackner. Vibration and crack detection in gas turbine engine compressor blades using eddy current sensors. Master's project, Massachusetts Institute of Technology, 2004.

[4] A. von Flotow, M. Mercadal, and P. Tappert. Health monitoring and prognostics of blades and disks with blade tip sensors. In *Aerospace Conference Proceedings, 2000 IEEE*, volume 6, pages 433–440 vol.6, 2000.

[5] M. Dowell, G. Sylvester, R. Krupp, and G. Zipfel. Progress in turbomachinery prognostics and health management via eddy-current sensing. In *Aerospace Conference Proceedings, 2000 IEEE*, volume 6, pages 133–143 vol.6, 2000.

[6] David Halliday, Robert Resnick, and Kenneth S. Krane. *Physics*, volume 2. John Wiley & Sons, fourth edition, 1992.

[7] G. Y. Tian, Z. X. Zhao, R. W. Baines, and P. Corcoran. Blind sensing [eddy current sensor]. *Manufacturing Engineer*, 76:179–182, 1997.

[8] Jin Au Kong. *Electromagnetic Wave Theory*. E M W Pub, 2000.

[9] Yu Yating, Du Pingan, and Wang Zhenwei. Study on the electromagnetic properties of eddy current sensor. In *Mechatronics and Automation, 2005 IEEE International Conference*, volume 4, pages 1970–1975, 2005.

[10] C. Teolis, D. Gent, C. Kim, A. Teolis, J. Paduano, and M. Bright. Eddy current sensor signal processing for stall detection. In *Aerospace, 2005 IEEE Conference*, pages 1–17, 2005.

[11] B. Lequesne, A. M. Pawlak, and T. Schroeder. Magnetic velocity sensors. *Industry Applications, IEEE Transactions on*, 32:1166–1175, 1996.

[12] John R. Gyorki. Strain sensor basics and signal conditioning tips. *Sensors*, 22(6):18–23, June 2005.

[13] Yiben Lin. Fabrication and testing of a spar-actuated active compressor rotor blade. Master's project, Massachusetts Institute of Technology, 2003.

[14] S. Heath and M. Imregun. An improved single-parameter tip-timing method for turbomachinery blade vibration measurements using optical laser probes. *International Journal of Mechanical Sciences*, 38(10):1047–1058, September 1995.

[15] Alan V. Oppenheim, Alan S. Willsky, with S. Hamid, and S. Hamid Nawab. *Signals and Systems*. Prentice Hall, second edition, 1996.

[16] Alan V. Oppenheim, Ronald W. Schafer, and John R. Buck. *Discrete-Time Signal Processing*. Prentice Hall, second edition, 1999.

[17] V. Cizek. Discrete hilbert transform. *Audio and Electroacoustics, IEEE Transactions on*, 18:340–343, 1970.

[18] M. A. Poletti. The homomorphic analytic signal. *Signal Processing, IEEE Transactions on*, 45:1943–1953, 1997.

[19] M. Sun and R. J. Sclabassi. Discrete-time instantaneous frequency and its computation. *Signal Processing, IEEE Transactions on*, 41:1867–1880, 1993.

[20] Lisha Sun, Minfen Shen, and F. H. Y. Chan. A method for estimating the instantaneous frequency of non-stationary heart sound signals. In *Neural Networks and Signal Processing, 2003. Proceedings of the 2003 International Conference on*, volume 1, pages 798–801 Vol.1, 2003.

[21] Ali H. Sayed. *Fundamentals of Adaptive Filtering*. Wiley-IEEE Press, 2003.